

Phase field modelling and computer implementation: a review

X. Zhuang^{1,2}, S. Zhou^{1,2,5*}, G.D. Huynh², P. Aérias⁴, T. Rabczuk³

1 Department of Geotechnical Engineering, College of Civil Engineering, Tongji University, Shanghai 200092, P.R. China

2 Institute of Continuum Mechanics, Leibniz University Hannover, Hannover 30167, Germany

3 Institute of Structural Mechanics, Bauhaus University Weimar, Weimar 99423, Germany

4 Department of Mechanical Engineering, Instituto Superior Técnico, University of Lisbon

5 Institute for Advanced Study, Tongji University, Shanghai 200092, P.R. China

* Corresponding author: Shuwei Zhou (shuwei.zhou@hot.uni-hannover.de)

Abstract

This paper presents an overview of the theories and computer implementation aspects of phase field models (PFM) of fracture. The advantage of PFM over discontinuous approaches to fracture is that PFM can elegantly simulate complicated fracture processes including fracture initiation, propagation, coalescence, and branching by using only a scalar field, the phase field. In addition, fracture is a natural outcome of the simulation and obtained through the solution of an additional differential equation related to the phase field. No extra fracture criteria are needed and an explicit representation of a crack surface as well as complex track crack procedures are avoided in PFM for fracture, which in turn dramatically facilitates the implementation. The PFM is thermodynamically consistent and can be easily extended to multi-physics problem by 'changing' the energy functional accordingly. Besides an overview of different PFMs, we also present comparative numerical benchmark examples to show the capability of PFMs.

Keywords: Phase field, Brittle fracture, Computer implementation, Finite element method, Hydraulic fracture

Contents

1 Introduction

4

2	Theories of phase field models for fracture	5
2.1	Physical models based on Landau-Ginzburg phase transition	5
2.1.1	Aranson, Kalastky, Vinokur model, 2000	5
2.1.2	Karma, Kessler, Levine model, 2001	6
2.1.3	Henry and Levine model, 2004	7
2.2	Mechanical models based on Griffith’s fracture theory	8
2.2.1	Variational approach to fracture	8
2.2.2	Kuhn and Müller model, 2008	9
2.2.3	Amor, Marigo, Maurini model, 2009	9
2.2.4	Miehe et al. model, 2010	10
2.3	Phase field approximation of the sharp crack topology	12
2.3.1	Classic crack surface density function	12
2.3.2	Generic geometric crack function	12
2.4	Energetic degradation function	15
2.4.1	Classic forms	15
2.4.2	Wu’s model, 2017	15
2.4.3	Sargado et al. model, 2017	16
2.5	On constitutive assumptions	16
2.6	Governing equations of PFM in strong form	17
2.7	Similarities and differences between gradient-damage and phase field methods	19
3	PFMs coupled with different discretization methods	20
3.1	Finite element method	20
3.2	Isogeometric method	20
3.3	Meshfree method	21
3.4	Physics informed neural network	22
3.5	FFT solver for phase field modeling	22
4	Finite element implementation of phase field methods	23
4.1	FE approximation	23
4.2	Solution schemes	25
4.2.1	Monolithic scheme	25
4.2.2	Staggered scheme	25
4.3	Implementation codes	26
4.3.1	Abaqus implementation	26
4.3.2	COMSOL implementation	26
4.3.3	FEniCS implementation	28
4.4	Computational cost	28

4.5	Element technologies	28
4.5.1	Adaptive mesh refinement	28
4.5.2	Multi-scale phase field method	29
4.5.3	New element shape function	30
4.5.4	Virtual element and smooth finite element	30
4.6	Special treatments	31
4.6.1	Modelling pre-existing cracks	31
4.6.2	Determining crack tip position	31
4.6.3	Hierarchical meshes	31
5	Extensions and applications of the PFMs	32
5.1	Ductile fracture	32
5.2	Cohesive fracture	33
5.3	Dynamic fracture	34
5.4	Finite deformation fracture	35
5.5	Anisotropic fracture	36
5.6	Plate and shell fractures	36
5.7	Thermal fracture	39
5.8	Hydraulic fracture	40
5.9	length scale insensitive phase-field model	42
5.10	Rock fracture	42
6	Representative numerical examples	43
6.1	Single-phasic problem	43
6.1.1	Quasi-static fracture	43
6.1.2	Dynamic fracture	51
6.2	Hydraulic fracture	54
6.2.1	Propagation of a single crack by internal fluid injection	54
6.2.2	Two parallel propagating cracks subjected to internal fluid injection	54
6.2.3	Three parallel propagating cracks in 2D	55
6.2.4	Propagation of two parallel penny-shaped cracks in 3D	55
6.3	Fractures in plates and shells	55
6.3.1	Single edge notched tension test	58
6.3.2	Simply supported Plate	58
6.3.3	Notched cylinder with internal pressure	59
7	Conclusions	62

1 Introduction

The prediction of material failure is of major importance in engineering and material science (Rabczuk 2013). Consequently, many numerical approaches have been developed to handle fracture problems in recent years. They can be classified into two categories namely discontinuous and continuous approaches. Discontinuous approaches introduce a strong discontinuity in the displacement field. Typical discontinuous methods are discrete crack models (Ingraffea and Saouma 1985), the extended finite element method (XFEM) (Moës and Belytschko 2002; Moës et al. 1999), generalized finite element method (GFEM) (Fries and Belytschko 2010), and the phantom-node method (Chau-Dinh et al. 2012; Rabczuk et al. 2008). Most discontinuous approaches to fracture require a method to represent the crack’s topology – such as triangular facets (Zhuang et al. 2012) or level sets (Zhuang et al. 2011) – and associated crack tracking algorithms. Obtaining complex fracture patterns such as crack branching and crack interactions require additional criteria (the TLS approach (Moës et al. 2011) is a discontinuous approach that does not require special criteria for branching). Some of the above methods also employ special schemes to ‘treat’ crack tip singularity, which improves accuracy but imposes other difficulties such as numerical integration.

In contrary to the discontinuous approaches, the continuous approaches to fracture do not introduce discontinuities in the displacement field. Popular continuous approaches include gradient damage models (Peerlings et al. 1996), screened-Poisson models (Areias et al. 2016a,b) and phase field models (PFMs) (Borden et al. 2012; Miehe et al. 2010a,b). All these models introduce an intrinsic length scale and smear the fracture over a localization band of finite width. This paper focuses on the phase field model of brittle fracture. Phase-field models of brittle fracture can be traced back to the late 1990s and received extensive development in theory and computer implementation. The crack is diffusively represented by a scalar field (phase field) and the evolution equation of the phase field is used to model crack propagation.

The phase field models recently received extensive attention because they can elegantly simulate complicated fracture processes including crack initiation, propagation, coalescence, and branching quite naturally. In addition, the fracture evolution can be simulated on a fixed mesh. The phase field model avoids the laborious task to track crack surface, which is especially tedious in 3D.

In the past decade, researchers made a huge effort to develop novel, efficient, and accurate phase field models and achieved enormous progress. This paper aims to review the advances in this direction. It is organized as follows. Section 2 gives an overview of the theories used in the phase field modelling. Section 3 is devoted to the different discretization methods in fracture modelling. Section 4 gives detailed FE discretization and some details about the computer implementation in phase field modeling. An overview of the state-of-the-art applications and extensions of the phase field models is given in Section 5 followed by Section 6 which presents

some representative numerical examples to show the capability and practicability of PFM in 2D and 3D. Finally, we end with concluding remarks and future directions in Section 7.

2 Theories of phase field models for fracture

In this section, we provide the basic theories of the phase field method for fractures. The phase field models are different in the ‘physics’ and ‘mechanics’ communities. The difference between these two models lies in that in the physics community, the models commonly come from the Landau-Ginzburg phase transition (Aranson et al. 2000) without introducing the idea of length scale to diffuse the crack. In addition, the free energy in the models don’t contain the fracture energy. The PFMs in the physics community are often used to model dynamic fractures (Aranson et al. 2000; Henry and Levine 2004; Karma et al. 2001). However, the phase field models in the mechanics community (Miehe et al. 2010a,b), can be regarded as the extension of Griffith’s fracture theory although the crack evolution is similar to the Landau-Ginzburg phase transition while a clear length scale parameter is used. The free energy used for variational analysis contains the fracture energy, which is regularized by using the length scale parameter.

2.1 Physical models based on Landau-Ginzburg phase transition

2.1.1 Aranson, Kalastky, Vinokur model, 2000

The fracture model presented by Aranson et al. (2000) is among the first phase-field like descriptions of crack propagation in brittle materials. Their model focuses on Mode-I fracture and they implemented their approach in 2D. The displacement \mathbf{u} satisfies the standard elastodynamic equation with a damping term:

$$\rho\ddot{\mathbf{u}} = \eta\Delta\dot{\mathbf{u}} + \nabla \cdot \boldsymbol{\sigma} \quad (1)$$

where ρ is the density of material, ∇ and Δ are the divergence and Laplace operators, $\boldsymbol{\sigma}$ is the stress tensor, $\eta > 0$ is a viscous damping parameter, $\dot{\mathbf{u}} = \partial\mathbf{u}/\partial t$, and $\ddot{\mathbf{u}} = \partial^2\mathbf{u}/\partial t^2$ with t being the time.

Aranson et al. (2000) defined a local-order parameter s (a field parameter): $s = 1$ outside the crack (no defects) and $s = 0$ inside the crack (all the atomic bonds are broken). The order parameter s is assumed much larger than the inter-atomic distance, thereby obeying the continuum description of fracture. Materials cannot bear tensile stresses and fail at an order parameter below the critical value s_c (Aranson et al. 2000). The stress-strain relation subsequently differs from that used in the isotropic linear elasticity $\boldsymbol{\sigma} = \mathbb{C} : \boldsymbol{\varepsilon}$ by introducing the dependency on the order parameter s :

$$\boldsymbol{\sigma} = s\mathbb{C} : \boldsymbol{\varepsilon} + \chi s\dot{\mathbf{I}} \quad (2)$$

where \mathbb{C} is fourth-order elasticity tensor of material, $\boldsymbol{\varepsilon}$ is the strain tensor, \mathbf{I} is the second-order identity tensor, and $\chi > 0$ is an additional material parameter describing the hydrostatic pressure due to creation of new defects.

The order parameter s is assumed to be governed by pure dissipative dynamics and $\dot{s} = -\delta E/\delta s$ with E being a "free-energy" type functional. Based on the Landau's phase transitions (Landau et al. 1980), the simplest form of E reads

$$E = \int_{\Omega} [P(s) + D_s |\nabla s|^2] \, d\Omega \quad (3)$$

where P is a polynomial functional and $D_s > 0$ is an adaptive constant.

In the fracture model of Aranson et al. (2000), the order parameter evolution equation is naturally expressed as

$$\dot{s} = D_s \Delta s - s(1-s) [a(1 + (\text{tr}(\boldsymbol{\varepsilon}) - b)s) - c \mathbf{i} \cdot \nabla s] \quad (4)$$

where a , b , and c are model parameters.

In general, the Aranson, Kalastky, Vinokur model can simulate multiple fracture behaviors such as crack initiation, propagation, branching, dynamic fracture instability, sound emission and fragmentation. However, some discrepancies still exist between the numerical predications and experimental observations of Mode I crack propagation in a rectangular strip of finite width (Aranson et al. 2000).

2.1.2 Karma, Kessler, Levine model, 2001

Karma et al. (2001) proposed a phase-field model for Mode III (antiplane shear) fracture. In their model, only the out-of-plane displacement component exists in a 2D setting. Their approach for fracture emanates from the original phase field models for solidification and the basic free energy function is expressed as (Hakim and Karma 2009; Karma et al. 2001)

$$E(\mathbf{u}, s) = \int_{\Omega} \left[g(s) (\Psi_0(\boldsymbol{\varepsilon}) - \Psi_c) + V(s) + \frac{1}{2} D_s |\nabla s|^2 \right] \, d\Omega \quad (5)$$

where $g(s)$ is a function of the order parameter s and satisfies $g(s) > 0$ for $0 < s \leq 1$. $V(s) = s^2(1-s^2)/4$ is the so-called Ginzburg-Landau double-well potential (Ambati et al. 2015b). In addition, Ψ_c denotes the strain energy threshold for crack initiation, and $D_s > 0$ is the positive constant identical to that in Eq. (3). Note that the function $g(s) = s^{2+a_1}$ is used in Karma et al. (2001) with a_1 a dimensionless coefficient. Subsequently, the energy functional is used to governing the main equations of systems, including the momentum balance equation, the stress-strain relation and the phase-field evolution equation.

That is, the variation of the functional E with respect to \mathbf{u} results in the equilibrium equation: $\rho \ddot{\mathbf{u}} = \nabla \cdot \boldsymbol{\sigma}$. The stress-strain form is subsequently represented as follows:

$$\boldsymbol{\sigma}(\mathbf{u}, s) = g(s) \frac{\partial \Psi_0(\boldsymbol{\varepsilon})}{\partial \boldsymbol{\varepsilon}} = g(s) \mathbb{C} : \boldsymbol{\varepsilon} \quad (6)$$

The proposed fracture evolution law reads $\tau \dot{s} = -\frac{\partial E(\mathbf{u}, s)}{\partial s}$ with $\tau \geq 0$ being a kinetic modulus. The nonlinear evolution equation is thus expressed as follows:

$$\tau \dot{s} = D_s \Delta s - V'(s) - g'(s) (\Psi_0(\boldsymbol{\varepsilon}) - \Psi_c) \quad (7)$$

2.1.3 Henry and Levine model, 2004

Henry and Levine (2004) subsequently extended the original model of Karma et al. (2001). A modification of the elastic energy is seen in Henry and Levine (2004) for better simulating the crack growth of Mode I and II under 2D plane strain condition. The total energy functional retains the basic structure of the Karma, Kessler, Levine model (KKL model) and still prevents the compressed region of the elastic body from cracking. The total energy is expressed as follows,

$$E(\mathbf{u}, s) = \int_{\Omega} \left[g(s) (\tilde{\Psi}(\boldsymbol{\varepsilon}) - \Psi_c) + V(s) + \frac{1}{2} D_s |\nabla s|^2 \right] d\Omega \quad (8)$$

where $\tilde{\Psi}(\boldsymbol{\varepsilon})$ is the modified elastic strain energy and it is identical to the standard elastic energy density for a positive volume strain. However, for a negative volume strain, a breaking symmetry term is introduced:

$$\tilde{\Psi}(\boldsymbol{\varepsilon}) = \begin{cases} \Psi_0(\boldsymbol{\varepsilon}) & \text{if } \text{tr}(\boldsymbol{\varepsilon}) > 0 \\ \Psi_0(\boldsymbol{\varepsilon}) - \frac{1}{2} a_2 K \text{tr}^2(\boldsymbol{\varepsilon}) & \text{if } \text{tr}(\boldsymbol{\varepsilon}) < 0 \end{cases} \quad (9)$$

where $\Psi_0(\boldsymbol{\varepsilon}) = \frac{1}{2} \lambda \varepsilon_{ii}^2 + \mu \varepsilon_{ij}^2$, λ and μ are Lamé constants, $K = (\lambda + \mu)/2$, and $a_2 > 1$ is an arbitrary coefficient. It should be noted that the coupling function $g(s)$ used in the model of Henry and Levine (2004) is different from that in Karma et al. (2001) and here $g(s) = (4 - 3s)s^3$.

The stress-strain relation used in Henry and Levine model is

$$\boldsymbol{\sigma}(\mathbf{u}, s) = g(s) \frac{\partial \tilde{\Psi}(\boldsymbol{\varepsilon})}{\partial \boldsymbol{\varepsilon}} \quad (10)$$

while the evolution equation of s is modified as

$$\tau \dot{s} = D_s \Delta s - V'(s) - g'(s) (\tilde{\Psi}(\boldsymbol{\varepsilon}) - \Psi_c) \quad (11)$$

In summary, the Henry and Levine model can accurately reproduce different behaviors of cracks such as branching, experimentally observed oscillating cracks, and well observed super-critical Hopf bifurcation (Henry and Levine 2004).

2.2 Mechanical models based on Griffith’s fracture theory

2.2.1 Variational approach to fracture

The original phase field models (Miehe et al. 2010a) in the mechanics community is developed independently for quasi-static fractures. These approaches originate from the variational approach of brittle fracture proposed by Francfort and Marigo (1998) and refer to the regularization formulation used by Bourdin et al. (2000).

Similar to the models in the physics community, the variational approach to fracture also requires constructing an energy functional that governs the entire fracture process. That is, crack initiation, propagation, and branching is a minimization of the energy functional (Francfort and Marigo 1998):

$$E(\mathbf{u}, \Gamma) = \int_{\Omega} \Psi_0(\boldsymbol{\varepsilon}) d\Omega + G_c \int_{\Gamma} dS \quad (12)$$

where G_c is the fracture toughness and also referred to as the critical energy release rate. $\Gamma \in \Omega$ is an admissible crack set and the displacement field \mathbf{u} is discontinuous across Γ .

To make the variational formulation amenable to a numerical implementation, Bourdin et al. (2000) proposed a regularized version of the variational formulation. Without treating the free discontinuity sets of the displacement field \mathbf{u} , an auxiliary scalar $s(\mathbf{x}, t)$ (\mathbf{x} the position vector) is employed to diffusely represent the sharp fracture geometry. Identical to the physical phase field models, the scalar field s continuously transits between $s = 1$ (intact material) and $s = 0$ (fully damaged material). The main advantage of introduction of the phase-field is that the representation of cracks is no longer mesh or geometry based (Kuhn 2013). The regularized approach can be easily implemented in a finite element framework and retain the main advantage of the variational formulation to model cracks. In the regularization formulation of Bourdin et al. (2000), the modified energy functional reads

$$E(\mathbf{u}, s) = \int_{\Omega} (s^2 + \eta) \Psi_0(\boldsymbol{\varepsilon}(\mathbf{u})) d\Omega + G_c \int_{\Omega} \left[\frac{1}{4\epsilon} (1 - s)^2 + \epsilon |\nabla s|^2 \right] d\Omega \quad (13)$$

where the parameter $0 < \eta \ll 1$ is used to avoid numerical singularity when the material is broken. Another parameter ϵ has the dimension of a length and controls the transition zone between the fully damaged and intact body. To obtain the displacement \mathbf{u} and phase field s , minimization of the modified energy functional is also required. It should be noted that the regularized approach can be recovered to the original variational approach to fracture when

$\epsilon \rightarrow 0$ in the sense of Γ -convergence (Braides 2006).

2.2.2 Kuhn and Müller model, 2008

Kuhn and Müller (2008) reinterpreted the crack variable as a phase field order parameter and they also regarded cracking as a phase transition problem. By applying the thermodynamics framework of order parameter based models, Kuhn and Müller (2008) reformulated the minimization problem in Eq. (13) and used the stress equilibrium equation $\nabla \cdot \boldsymbol{\sigma} = \mathbf{0}$ with

$$\boldsymbol{\sigma} = (s^2 + \eta) \frac{\partial \Psi_0(\boldsymbol{\varepsilon})}{\partial \boldsymbol{\varepsilon}} = (s^2 + \eta) \mathbb{C} : \boldsymbol{\varepsilon} \quad (14)$$

The crack propagation is simulated by using the evolution equation of the order parameter s . The Ginzburg-Landau type evolution equation (Kuhn and Müller 2008) then reads

$$\dot{s} = -\dot{M} \left[2s\Psi_0(\boldsymbol{\varepsilon}) - G_c \left(2\epsilon\Delta s + \frac{1-s}{2\epsilon} \right) \right] \quad (15)$$

Equation (15) is used under the irreversibility constraint of crack evolution and with a mobility parameter M . $M \geq 0$ governs the dissipation of stable crack propagation. At a finite value of M , the crack model can be also regarded as a viscous quasi-static model (Miehe et al. 2010a) and in a limit case $M \rightarrow \infty$ quasi-static crack propagation thereby obeys

$$2s\Psi_0(\boldsymbol{\varepsilon}) - G_c \left(2\epsilon\Delta s + \frac{1-s}{2\epsilon} \right) = 0 \quad (16)$$

In Kuhn and Müller (2008), the numerical model is implemented within the finite element framework and an implicit Euler scheme is used for time integration. Note that the Kuhn and Müller model (Kuhn and Müller 2008) has the similar forms and derivations of the Karma, Kessler, Levine model (Karma et al. 2001) and Henry and Levine model (Henry and Levine 2004).

2.2.3 Amor, Marigo, Maurini model, 2009

The originally developed phase field model (e.g. Eq. (13)) does not distinguish between fractures due to compression and tension. Therefore, some unrealistic crack patterns are reported in Bourdin et al. (2000). To avoid unrealistic simulations, elastic energy must be decomposed into different parts. Amor et al. (2009) made the preliminary contribution to prevent phase field representation of cracks due to compression. Amor et al. (2009) modified the regularized formulation of Eq. (13) by introducing an additional decomposition of the elastic energy $\Psi_0(\boldsymbol{\varepsilon})$

into volumetric and deviatoric parts. That is, $\Psi_0 = \Psi_0^+ + \Psi_0^-$ with

$$\begin{cases} \Psi_0^+(\boldsymbol{\varepsilon}) = \frac{1}{2}K_n \langle \text{tr}(\boldsymbol{\varepsilon}) \rangle_+^2 + \mu(\boldsymbol{\varepsilon}^D : \boldsymbol{\varepsilon}^D) \\ \Psi_0^-(\boldsymbol{\varepsilon}) = \frac{1}{2}K_n \langle \text{tr}(\boldsymbol{\varepsilon}) \rangle_-^2 \end{cases} \quad (17)$$

where $K_n = \lambda + \mu$, $\boldsymbol{\varepsilon}^D = \boldsymbol{\varepsilon} - \frac{1}{3}\text{tr}(\boldsymbol{\varepsilon})\mathbf{I}$, and operators $\langle * \rangle_{\pm} = \frac{1}{2}(* \pm | * |)$. Amor et al. (2009) subsequently proposed the modified energy functional as

$$E(\mathbf{u}, s) = \int_{\Omega} ((s^2 + \eta)\Psi_0^+(\boldsymbol{\varepsilon}) + \Psi_0^-(\boldsymbol{\varepsilon})) \, d\Omega + G_c \int_{\Omega} \left[\frac{1}{4\epsilon}(1-s)^2 + \epsilon|\nabla s|^2 \right] \, d\Omega \quad (18)$$

Amor et al. (2009) applied an alternate minimization algorithm to solve for the energy functional (18) and achieved local minimization. They solved a series of minimization sub-problems on \mathbf{u} at a fixed s , and vice versa on s at a fixed \mathbf{u} until convergence. Ambati et al. (2015b) pointed out that a good outcome of the energy split of Ψ_0 is the resulting stress-strain relation:

$$\begin{aligned} \boldsymbol{\sigma}(\mathbf{u}, s) &= (s^2 + \eta) \frac{\partial \Psi_0^+}{\partial \boldsymbol{\varepsilon}} + \frac{\partial \Psi_0^-}{\partial \boldsymbol{\varepsilon}} \\ &= (s^2 + \eta) [K_n \langle \text{tr}(\boldsymbol{\varepsilon}) \rangle_+ \mathbf{I} + 2\mu \boldsymbol{\varepsilon}^D] + K_n \langle \text{tr}(\boldsymbol{\varepsilon}) \rangle_- \end{aligned} \quad (19)$$

However, the phase evolution equation suggested by Ambati et al. (2015b) is not the variational outcome of the energy functional (18). Instead, the Ginzburg-Landau type equation is still used and Ψ_0 in Eq. (15) is replaced by Ψ_0^+ :

$$\dot{s} = -\dot{M} \left[2s\Psi_0^+(\boldsymbol{\varepsilon}) - G_c \left(2\epsilon\Delta s + \frac{1-s}{2\epsilon} \right) \right] \quad (20)$$

Thus, the evolution of s in Eq. (20) is driven only by the positive parts of the elastic energy. That is, only volumetric dilatation and shear deformation can produce cracks. It should be noted here that the Amor, Marigo, Maurini model does not obey the Γ -convergence although the energy decomposition model (Amor et al. 2009) produces adequate numerical results. The reason is that it is not clear what kind of functional and physical process are to be recovered when $\epsilon \rightarrow \infty$.

2.2.4 Miehe et al. model, 2010

Miehe et al. (2010a,b) presented a thermodynamically consistent phase field model of brittle fracture. The model of Miehe et al. (2010a,b) is another important development after the variational framework of fracture was presented by Francfort and Marigo (1998) and Bourdin et al. (2000). This model is based on continuum mechanics and uses an auxiliary scalar field $\phi \in [0, 1]$ (the so-called phase field). The additional phase field is used to smear the sharp

crack shape. We can also regard $\phi = 1 - s$ here with relation to the former phase field models such as the Amor, Marigo, Maurini model. $\phi = 0$ and $\phi = 1$ represent the intact and fully broken states, respectively. A length scale parameter l_0 is used in Miehe et al. model and l_0 controls the transition region between the fully broken and intact bodies. Another elastic energy decomposition method is used with $\Psi_0 = \Psi_0^+ + \Psi_0^-$ based on the spectral decomposition of strain tensor $\boldsymbol{\varepsilon}$: $\boldsymbol{\varepsilon} = \sum_{I=1}^3 \varepsilon_I \mathbf{n}_I \otimes \mathbf{n}_I$. $\{\varepsilon\}_{I=1}^3$ and $\{\mathbf{n}\}_{I=1}^3$ are the principal strains and their directions. The decomposed elastic energy reads

$$\Psi_0^\pm(\boldsymbol{\varepsilon}) = \frac{1}{2} \lambda \langle \text{tr}(\boldsymbol{\varepsilon}) \rangle_\pm^2 + \mu \text{tr}(\boldsymbol{\varepsilon}_\pm^2) \quad (21)$$

where $\boldsymbol{\varepsilon}_\pm = \sum_{I=1}^3 \langle \varepsilon_I \rangle_\pm \mathbf{n}_I \otimes \mathbf{n}_I$.

The modified elastic energy Ψ_e used in the total energy functional is expressed as follows,

$$\Psi_e = [(1 - \phi)^2 + \eta] \Psi_0^+ + \Psi_0^- \quad (22)$$

The governing equation of the displacement is $\nabla \cdot \boldsymbol{\sigma} = \mathbf{0}$ and the stress tensor is expressed as

$$\boldsymbol{\sigma}(\mathbf{u}, \phi) = [(1 - \phi)^2 + \eta] \frac{\partial \Psi_0^+}{\partial \boldsymbol{\varepsilon}} + \frac{\partial \Psi_0^-}{\partial \boldsymbol{\varepsilon}} \quad (23)$$

The evolution equation of phase field in the model of [Miehe et al. \(2010a,b\)](#) is

$$\xi \dot{\phi} = 2(1 - \phi) \Psi_0^+(\boldsymbol{\varepsilon}) + \frac{G_c}{l_0} (\phi - l_0^2 \Delta \phi) \quad (24)$$

where ξ is a viscosity parameter.

It should be noted that if $l_0 = 2\epsilon$ and $\xi = \frac{1}{M}$, the structure of Eqs. (23) and (24) resembles those equations in the Amor, Marigo, Maurini model ([Amor et al. 2009](#)). The energy decomposition of [Miehe et al. \(2010a,b\)](#) is different from that of [Amor et al. \(2009\)](#). [Miehe et al. \(2010a,b\)](#) only distinguishes compressive and tensile parts and imposed a degradation of the compressive energy component. However, the deviatoric stress is considered in [Amor et al. \(2009\)](#). Another feature of Miehe's model is that Eq. (23) results in a highly non-linear stress-strain relationship. Therefore, a much higher computational cost is needed compared with former physical and mechanical phase field methods. In order to ensure a monotonically increasing phase-field, the irreversibility condition must be imposed as a constraint during compression or unloading. [Miehe et al. \(2010a,b\)](#) proposed a new approach where a history-field H is defined in a loading process:

$$H(\mathbf{x}, t) = \max_{\tau \in [0, t]} \psi_0^+(\boldsymbol{\varepsilon}(\mathbf{x}, \tau)) \quad (25)$$

The introduction of the history field enhances the phase-field formulations and overcomes some implementation difficulties. Replacing Ψ_0^+ in Eq. (24) by H , the finally used evolution

equation reads

$$\xi \dot{\phi} = 2(1 - \phi)H + \frac{G_c}{l_0} (\phi - l_0^2 \Delta \phi) \quad (26)$$

The common isotropic, anisotropic, and hybrid phase field models in the mechanics community are summarized in Table 1. Thus, the differences in governing equations and driving forces for different PFMs can be easily identified by readers.

2.3 Phase field approximation of the sharp crack topology

2.3.1 Classic crack surface density function

For the crack phase field $s(\mathbf{x}, t)$ or $\phi(\mathbf{x}, t)$, let us follow [Miehe et al. \(2010a,b\)](#) and introduce a regularized functional $A(\phi)$ or $A(s)$ such that

$$\begin{cases} A_d(\phi) = \int_{\Omega} \gamma(\phi, \nabla \phi) d\Omega \approx \int_{\Omega} \delta_s d\Omega = \int_{\Gamma} dS = A_s \\ A_d(s) = \int_{\Omega} \gamma(s, \nabla s) d\Omega \approx \int_{\Omega} \delta_s d\Omega = \int_{\Gamma} dS = A_s \end{cases} \quad (27)$$

where $\gamma(\phi, \nabla \phi)$ or $\gamma(s, \nabla s)$ is the crack surface density function, and A_s is the crack area. The crack surface density function approximates the Dirac-delta δ_s along the crack Γ , and is composed of the crack phase-field and its spatial gradient.

[Bourdin et al. \(2000\)](#) proposed the original form of the crack surface density function as

$$\gamma(s, \nabla s) = \frac{1}{4\epsilon} (1 - s)^2 + \epsilon |\nabla s|^2 \quad (28)$$

[Miehe et al. \(2010a,b\)](#) followed the original form of [Bourdin et al. \(2000\)](#) but used different parameters and phase field:

$$\gamma(\phi, \nabla \phi) = \frac{1}{2l_0} \phi^2 + \frac{l_0}{2} |\nabla \phi|^2 \quad (29)$$

In the physical phase field models, the crack surface density function follows a Ginzburg-Landau double-well potential ([Hakim and Karma 2009](#); [Karma et al. 2001](#)):

$$\gamma(s, \nabla s) = \frac{s^2(1 - s^2)}{4} + \frac{1}{2} D_s |\nabla s|^2 \quad (30)$$

2.3.2 Generic geometric crack function

Kuhn, Schlüter, Müller model, 2015 [Kuhn et al. \(2015\)](#) proposed a generic energy density functional Ψ of a phase field fracture model:

$$\Psi = (g(s) + \eta) \Psi_0 + \frac{G_c}{2c_w} \left(\frac{w(s)}{4\epsilon} + \epsilon |\nabla s|^2 \right) \quad (31)$$

Table 1: Different forms of phase field methods in mechanics community

Type	Governing equations	Definition
Isotropic	$\begin{cases} \nabla \cdot \boldsymbol{\sigma} + \mathbf{b} = 0 \\ -l_0^2 \Delta \phi + \phi = \frac{2l_0}{G_c} (1 - \phi) H \\ \boldsymbol{\sigma}(\mathbf{u}, \phi) = (1 - \phi)^2 \frac{\partial \psi_0}{\partial \boldsymbol{\varepsilon}} \\ \mathbb{D} = \frac{\partial \boldsymbol{\sigma}}{\partial \boldsymbol{\varepsilon}} \end{cases}$	$\begin{aligned} H &= \max_{\tau \in [0, t]} \psi_0(\boldsymbol{\varepsilon}(\mathbf{x}, \tau)) \text{ with} \\ \psi_0 &= \frac{\lambda}{2} (\text{tr}(\boldsymbol{\varepsilon}))^2 + \mu \text{tr}(\boldsymbol{\varepsilon}^2) \end{aligned}$
Anisotropic (Miehe et al. 2010a)	$\begin{cases} \nabla \cdot \boldsymbol{\sigma} + \mathbf{b} = 0 \\ \left(\frac{2l_0 H}{G_c} + 1 \right) \phi - l_0^2 \nabla^2 \phi = \frac{2l_0 H}{G_c} \\ \boldsymbol{\sigma}(\mathbf{u}, \phi) = (1 - \phi)^2 \frac{\partial \psi_\varepsilon^+}{\partial \boldsymbol{\varepsilon}} + \frac{\partial \psi_\varepsilon^-}{\partial \boldsymbol{\varepsilon}} \\ \mathbb{D} = \frac{\partial \boldsymbol{\sigma}^+}{\partial \boldsymbol{\varepsilon}} + \frac{\partial \boldsymbol{\sigma}^-}{\partial \boldsymbol{\varepsilon}} \end{cases}$	$\begin{aligned} H &= \max_{\tau \in [0, t]} \psi_\varepsilon^+(\boldsymbol{\varepsilon}(\mathbf{x}, \tau)), \\ \boldsymbol{\sigma}^+ &= (1 - \phi)^2 \frac{\partial \psi_\varepsilon^+}{\partial \boldsymbol{\varepsilon}}, \quad \boldsymbol{\sigma}^- = \frac{\partial \psi_\varepsilon^-}{\partial \boldsymbol{\varepsilon}}, \\ \psi_\varepsilon^\pm(\boldsymbol{\varepsilon}) &= \frac{\lambda}{2} (\text{tr}(\boldsymbol{\varepsilon}))_\pm^2 + \mu \text{tr}(\boldsymbol{\varepsilon}_\pm^2) \end{aligned}$
Anisotropic (Amor et al. 2009)	$\begin{cases} \nabla \cdot \boldsymbol{\sigma} + \mathbf{b} = 0 \\ -l_0^2 \Delta \phi + \phi = \frac{2l_0}{G_c} (1 - \phi) H \\ \boldsymbol{\sigma}(\mathbf{u}, \phi) = (1 - \phi)^2 \frac{\partial \psi_0^+}{\partial \boldsymbol{\varepsilon}} + \frac{\partial \psi_0^-}{\partial \boldsymbol{\varepsilon}} \\ \mathbb{D} = \frac{\partial \boldsymbol{\sigma}^+}{\partial \boldsymbol{\varepsilon}} + \frac{\partial \boldsymbol{\sigma}^-}{\partial \boldsymbol{\varepsilon}} \end{cases}$	$\begin{aligned} H &= \max_{\tau \in [0, t]} \psi_0^+(\boldsymbol{\varepsilon}(\mathbf{x}, \tau)), \\ \boldsymbol{\sigma}^+ &= (1 - \phi)^2 \frac{\partial \psi_0^+}{\partial \boldsymbol{\varepsilon}}, \quad \boldsymbol{\sigma}^- = \frac{\partial \psi_0^-}{\partial \boldsymbol{\varepsilon}}, \\ \psi_0^+ &= \frac{1}{2} K_n \langle (\text{tr}(\boldsymbol{\varepsilon}))_+^2 + \mu(\boldsymbol{\varepsilon}^{\text{dev}} : \boldsymbol{\varepsilon}^{\text{dev}}) \rangle, \\ \psi_0^- &= \frac{1}{2} K_n \langle (\text{tr}(\boldsymbol{\varepsilon}))_-^2 \rangle \text{ with } K_n \text{ a physical parameter} \end{aligned}$
Hybrid (Ambati et al. 2015b)	$\begin{cases} \nabla \cdot \boldsymbol{\sigma} + \mathbf{b} = 0 \\ -l_0^2 \Delta \phi + \phi = \frac{2l_0}{G_c} (1 - \phi) H \\ \boldsymbol{\sigma}(\mathbf{u}, \phi) = (1 - \phi)^2 \frac{\partial \psi_0}{\partial \boldsymbol{\varepsilon}} \\ \mathbb{D} = \frac{\partial \boldsymbol{\sigma}}{\partial \boldsymbol{\varepsilon}} \end{cases}$	$\begin{aligned} H &= \max_{\tau \in [0, t]} \psi_\varepsilon^+(\boldsymbol{\varepsilon}(\mathbf{x}, \tau)), \\ \psi_0 &= \frac{\lambda}{2} (\text{tr}(\boldsymbol{\varepsilon}))^2 + \mu \text{tr}(\boldsymbol{\varepsilon}^2), \\ \psi_\varepsilon^+(\boldsymbol{\varepsilon}) &= \frac{\lambda}{2} (\text{tr}(\boldsymbol{\varepsilon}))_+^2 + \mu \text{tr}(\boldsymbol{\varepsilon}_+^2) \end{aligned}$
Hybrid (Zhang et al. 2017)	$\begin{cases} \nabla \cdot \boldsymbol{\sigma} + \mathbf{b} = 0 \\ (1 - \phi) \left(\frac{H_1}{G_{cI}} + \frac{H_2}{G_{cII}} \right) - \frac{1}{2l_0} \phi + \frac{l_0}{2} \Delta \phi = 0 \\ \boldsymbol{\sigma}(\mathbf{u}, \phi) = (1 - \phi)^2 \frac{\partial \psi_0}{\partial \boldsymbol{\varepsilon}} \\ \mathbb{D} = \frac{\partial \boldsymbol{\sigma}}{\partial \boldsymbol{\varepsilon}} \end{cases}$	$\begin{aligned} H_1 &= \max_{\tau \in [0, t]} \lambda (\text{tr}(\boldsymbol{\varepsilon}))_+^2, \\ H_2 &= \max_{\tau \in [0, t]} \mu \text{tr}[\langle \boldsymbol{\varepsilon} \rangle_+^2], \quad G_{cI} \text{ and } G_{cII} \\ &\text{are the critical energy release rate of} \\ &\text{modes I and II} \end{aligned}$
Hybrid (Zhou et al. 2019a)	$\begin{cases} \nabla \cdot \boldsymbol{\sigma} + \mathbf{b} = 0 \\ -l_0^2 \Delta \phi + \phi = \frac{2l_0}{G_c} (1 - \phi) H \\ \boldsymbol{\sigma}(\mathbf{u}, \phi) = (1 - \phi)^2 \frac{\partial \psi_0}{\partial \boldsymbol{\varepsilon}} \\ \mathbb{D} = \frac{\partial \boldsymbol{\sigma}}{\partial \boldsymbol{\varepsilon}} \end{cases}$	$\begin{aligned} H &= \max_{\tau \in [0, t]} \psi_p(\boldsymbol{\varepsilon}(\mathbf{x}, \tau)), \quad \psi_p = \\ &\sum_{i=j+1}^3 \sum_{j=1}^2 \frac{1}{2G} \left\langle \frac{\mu(\varepsilon_{ip} - \varepsilon_{jp})}{\cos \varphi} \right\rangle + [\lambda(\varepsilon_{1p} + \\ &+ \varepsilon_{2p} + \varepsilon_{3p}) + \mu(\varepsilon_{ip} + \varepsilon_{jp})] \tan \varphi - c \Big _+^2 \end{aligned}$

where $g(s)$ is the energetic degradation function with $g(1) = 1$ and $g(0) = 0$. The function $w(s)$ models the local fracture energy and c_w is a normalization constant that results in the integral of $\left(\frac{w(s)}{4\epsilon} + \epsilon|\nabla s|^2\right)/(2c_w)$ over the fractured domain converges to the surface measure of the crack set when $\epsilon \rightarrow 0$ (Kuhn et al. 2015). Kuhn et al. (2015) concluded two types of $w(s)$, namely, the double well function $w(s) = 16s^2(1 - s^2)$ and monotonous functions $w(s) = (1 + \beta s)(1 - s)$ with $\beta \in [-1, 1]$. The convex quadratic function with $\beta = -1$ is mostly used, such as in the model of Miehe et al. (2010a). In addition, models with $\beta = 0$ can be found in Hossain et al. (2014).

Kuhn (2013) compared the function of $w(s) = 16s^2(1 - s^2)$ and $w(s) = (1 - s)^2$. The function $w(s)$ of these two forms is shown in Fig. 1. Their observations proved that the double well potential naturally models the irreversibility of fracture processes to a certain extent because of local maximum acting as an energy barrier between the broken and undamaged phase. In contrast, the crack phase field needs additional irreversibility to prevent crack healing for $w(s) = (1 - s)^2$ due to lack of energy barrier between the broken and undamaged states.

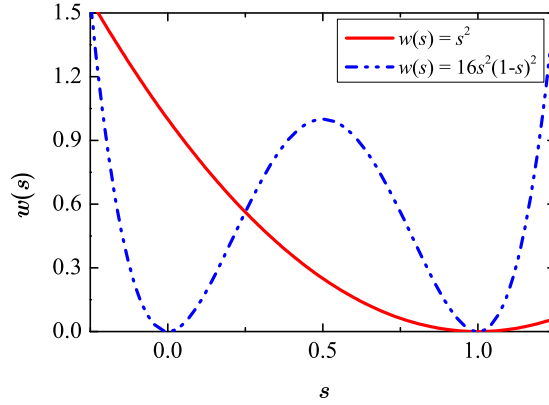


Fig. 1 Different degradation functions

Wu's model, 2017 Wu (2017) proposed another generic form for the crack surface density function $\gamma(\phi, \nabla\phi)$:

$$\gamma(\phi, \nabla\phi) = \frac{1}{c_0} \left(\frac{1}{b} \kappa(\phi) + b |\nabla\phi|^2 \right) \quad (32)$$

with

$$c_0 = 4 \int_0^1 \sqrt{\kappa(\beta)} d\beta \quad (33)$$

where $\kappa(\phi)$ is the geometric function that characterizes homogeneous evolution of the crack phase-field, b is an internal length scale parameter that regularizes the sharp crack, $c_0 > 0$ is a scaling parameter by which the regularized functional $A_d(\phi)$ can be recovered to the crack

surface A_s when $b \rightarrow 0$. The proposed crack geometric function $\kappa(\phi)$ must obey

$$\kappa(0) = 0, \quad \text{and} \quad \kappa(1) = 1 \quad (34)$$

2.4 Energetic degradation function

2.4.1 Classic forms

As aforementioned, $g(s)$ is a degradation function that models the degradation of the elastic energy when a fracture initiates. Seen from a simple stress-strain relation $\boldsymbol{\sigma} = (g(s) + \eta)\boldsymbol{\varepsilon}$, the function $g(s)$ also models the decrease in the stiffness in a broken material when the phase field $s \rightarrow 0$. In addition, the energetic degradation function $g(s)$ must monotonically increase with $g(1) = 1$ and $g(0) = 0$. Because the derivative $g'(s)$ enters the evolution equation of the phase field, $g'(0) = 0$ must be imposed to eliminate the elastic driving term $\frac{\partial \Psi}{\partial s} = \frac{1}{2}g'(s)\boldsymbol{\varepsilon} : \boldsymbol{\varepsilon}$ when $s = 0$.

Some of the classic degradation functions have been mentioned in the overview of the most important phase field models such as the quadratic function $g(s) = s^2$ in Bourdin et al. (2000), and the quartic function $g(s) = 4s^3 - 3s^4$ in the KKL model (Karma et al. 2001). In addition, Kuhn et al. (2015) adopted a cubic function:

$$g(s) = 3s^2 - 2s^3 \quad (35)$$

2.4.2 Wu's model, 2017

Wu (2017) proposed a unified phase field damage model for brittle fracture. The elastic energy density Ψ is modeled as

$$\Psi = v(\phi)\Psi_0 \quad (36)$$

The monotonically decreasing energetic function $v(\phi)$ describes degradation of the initial energy Ψ_0 with the crack phase-field evolution. The function $v(\phi)$ obeys (Miehe et al. 2010a)

$$v'(\phi) < 0, \quad \text{and} \quad v(0) = 1, \quad v(1) = 0, \quad v'(1) = 0 \quad (37)$$

The generic form of the energetic degradation function proposed by Wu (2017) is given by

$$v(\phi) = \frac{(1 - \phi)^{p_1}}{(1 - \phi)^{p_1} + Q(\phi)} \quad (38)$$

with the exponent $p_1 > 0$ and continuous function $Q(\phi) > 0$.

For a strictly positive function $Q(\phi)$, the following polynomial is considered

$$Q(\phi) = \alpha_1\phi + \alpha_1\alpha_2\phi^2 + \alpha_1\alpha_2\alpha_3\phi^3 + \dots = \alpha_1\phi P(\phi) \quad (39)$$

$$P(\phi) = 1 + \alpha_2\phi + \alpha_2\alpha_3\phi^2 + \dots \quad (40)$$

More details about the determination of the coefficients $\alpha_1, \alpha_2, \dots$ can be referred to [Wu \(2017\)](#).

2.4.3 Sargado et al. model, 2017

[Sargado et al. \(2017\)](#) proposed a new parametric family of degradation functions to increase the accuracy of phase field models in predicting critical loads. Expect a better prediction of the crack initiation and propagation, their additional goal is to preserve linear elastic response in the bulk material prior to fracture. Their numerical examples indicated the superiority of the proposed family of functions to the classical quadratic degradation function.

The family of degradation functions proposed by [Sargado et al. \(2017\)](#) are based on three parameters:

$$g_e(\phi) = (1 - w) \frac{1 - e^{-k(1-\phi)^n}}{1 - e^{-k}} + w f_c(\phi) \quad (41)$$

where k, n and w are parameters and $k > 0, n \geq 2$ and $w \in [0, 1]$. The function f_c acts as a corrector term. If $w = 0$, the proposed function has only two parameters and follows (a) $g_e(\phi)$ is monotonically decreasing, (b) $g_e(0) = 1, g_e(1) = 0$, and (c) $g'_e < 0, g'_e(1) = 0$.

2.5 On constitutive assumptions

As aforementioned, the model of [Amor et al. \(2009\)](#) and the model of [Miehe et al. \(2010a,b\)](#) achieve variationally consistent constitutive model for stress. In addition, the crack driving force D_s in the model of [Amor et al. \(2009\)](#) is derived by consistent variation:

$$D_s = \frac{1}{2} K_n \langle \text{tr}(\boldsymbol{\varepsilon}) \rangle_+^2 + \mu (\boldsymbol{\varepsilon}^D : \boldsymbol{\varepsilon}^D) \quad (42)$$

Consequently, only positive volume changes and distortion of the shape can produce crack evolution. For the model of [Miehe et al. \(2010a,b\)](#), the crack driving force D_s :

$$D_s = \frac{1}{2} \lambda \langle \text{tr}(\boldsymbol{\varepsilon}) \rangle_+^2 + \mu \text{tr}(\boldsymbol{\varepsilon}_+^2) \quad (43)$$

Both volumetric-deviatoric splits ([Amor et al. 2009](#)) and spectral decomposition ([Miehe et al. 2010a,b](#)) fully preserve the variational character of the phase field method. The energy split scheme ensures the energy contribution in the evolution of phase field and the non-

interpenetration condition on crack surfaces. This means that the normal stress on the crack should be non-positive and the shear stresses along a frictionless crack should vanish (Strobl and Seelig 2016). On this, some variationally non-consistent constitutive equations for the stress are developed. A constitutive model based on a crack orientation dependent decomposition of $\boldsymbol{\sigma}$ is mentioned in Strobl and Seelig (2016) where $\boldsymbol{\sigma}_a$ and $\boldsymbol{\sigma}_p$ represent the stress affected and unaffected by the phase field respectively. The stress decomposition depends on the normal strain ε_{nn} :

$$\begin{cases} \boldsymbol{\sigma}_a = g(s)(\lambda \text{tr}(\boldsymbol{\varepsilon})\mathbf{1} + 2\mu\boldsymbol{\varepsilon}), & \text{if } \varepsilon_{nn} > 0 \\ \boldsymbol{\sigma}_p = g(s)(\lambda \text{tr}(\boldsymbol{\varepsilon})\mathbf{1} + 2\mu\boldsymbol{\varepsilon}) + (1 - g(s))(\lambda + 2\mu)(\boldsymbol{\varepsilon} : \mathbf{N})\mathbf{N}, & \text{if } \varepsilon_{nn} < 0 \end{cases} \quad (44)$$

where $\mathbf{N} = \mathbf{n}_s \otimes \mathbf{n}_s$ with \mathbf{n}_s being the normal vector of the crack surface.

A more sophisticated stress model can be seen in Strobl and Seelig (2015) and only the stiffness normal to the crack is degraded. Tensile and shear stresses vanish on the fully developed crack surfaces. This results in the following stress:

$$\begin{aligned} \boldsymbol{\sigma}_a = & \left(\lambda + (g(s) - 1) \frac{\lambda^2}{\lambda + 2\mu} \right) \text{tr}(\boldsymbol{\varepsilon})\mathbf{1} + 2\mu\boldsymbol{\varepsilon} + (g(s) - 1) \left(\lambda + \frac{\lambda^2}{\lambda + 2\mu} \right) (\text{tr}(\boldsymbol{\varepsilon})\mathbf{N} + (\boldsymbol{\varepsilon} : \mathbf{N})\mathbf{1}) \\ & + 4(1 - g(s)) \left(\lambda + 2\mu - \frac{\lambda^2}{\lambda + 2\mu} \right) (\boldsymbol{\varepsilon} : \mathbf{N})\mathbf{N} + \mu(g(s) - 1)(\mathbf{N} \cdot \boldsymbol{\varepsilon} + \boldsymbol{\varepsilon} \cdot \mathbf{N}) \end{aligned} \quad (45)$$

For compression, only shear stresses parallel to the crack surfaces are degraded. The modified tensor is expressed as

$$\boldsymbol{\sigma}_p = \lambda \text{tr}(\boldsymbol{\varepsilon})\mathbf{1} + 2\mu\boldsymbol{\varepsilon} + 4\mu(1 - g(s))(\boldsymbol{\varepsilon} : \mathbf{N})\mathbf{N} + \mu(g(s) - 1)(\mathbf{N} \cdot \boldsymbol{\varepsilon} + \boldsymbol{\varepsilon} \cdot \mathbf{N}) \quad (46)$$

Equation (46) shows a transverse isotropy with symmetry about the crack normal and the stiffness degradation is described by λ , μ and the phase field.

2.6 Governing equations of PFM in strong form

In summary, the quasi-static phase-field models, which are developed from the regularized variational formulation of Bourdin et al. (2000), can be classified into three basic types, namely, the isotropic, anisotropic, and hybrid (isotropic-anisotropic) types. The isotropic and anisotropic formulations are the natural results of the variational principle and the basic structures can be expressed as follows.

(1) Isotropic formulation

$$\begin{cases} \nabla \cdot \boldsymbol{\sigma} + \mathbf{b} = 0 \\ -l_0^2 \phi \Delta \phi + \phi = \frac{2l_0}{G_c} (1-d)H \end{cases} \quad (47)$$

where $\boldsymbol{\sigma}(\mathbf{u}, \phi) = (1 - \phi)^2 \frac{\partial \Psi_0}{\partial \boldsymbol{\varepsilon}}$ and $H = \max_{\tau \in [0, t]} \psi_0(\boldsymbol{\varepsilon}(\mathbf{x}, \tau))$.

(2) Anisotropic formulation

$$\begin{cases} \nabla \cdot \boldsymbol{\sigma} + \mathbf{b} = 0 \\ -l_0^2 \phi \Delta \phi + \phi = \frac{2l_0}{G_c} (1-d)H^+ \end{cases} \quad (48)$$

where $\boldsymbol{\sigma}(\mathbf{u}, \phi) = (1 - \phi)^2 \frac{\partial \Psi_0^+}{\partial \boldsymbol{\varepsilon}} + \frac{\partial \Psi_0^-}{\partial \boldsymbol{\varepsilon}}$ and $H^+ = \max_{\tau \in [0, t]} \psi_0^+(\boldsymbol{\varepsilon}(\mathbf{x}, \tau))$.

It should be noted again that the isotropic formulation is easier to implement and has lower computational cost than the anisotropic formulation because the stress-strain constitutive relationship is linear in the isotropic approach. However, non-linear stress-strain relation exists in the anisotropic formulation. Despite of the lower implementation cost, the isotropic formulation can be used only in some very simple problems because fractures in compression and interpenetration of the crack faces are allowed. The anisotropic formulation which uses energy split technology, naturally overcomes the drawbacks emanating from the isotropic formulation. However, because of non-linearity from strain decomposition, the numerical implementation of the anisotropic models is laborious.

Ambati et al. (2015b) developed the hybrid phase field method, which retains a linear momentum balance equation. Thus, a favorable computational cost of the isotropic methods is retained. However, the evolution equation of the anisotropic methods is also retained to avoid fractures in compression. The hybrid model of Ambati et al. (2015b) reads

$$\begin{cases} \nabla \cdot \boldsymbol{\sigma} + \mathbf{b} = 0 \\ -l_0^2 \phi \Delta \phi + \phi = \frac{2l_0}{G_c} (1-d)H^+ \\ \boldsymbol{\sigma}(\mathbf{u}, \phi) = (1 - \phi)^2 \frac{\partial \Psi_0}{\partial \boldsymbol{\varepsilon}} \\ \forall \mathbf{x} : \Psi_0^+ < \Psi_0^- \rightarrow \phi = 0 \end{cases} \quad (49)$$

Wu (2017) also used the hybrid formulation but the driving force of the crack field is modified as

$$D_s = \frac{1}{2E_0} \bar{\sigma}_{eq} \quad (50)$$

where E_0 is the undamaged Young's modulus and $\bar{\sigma}_{eq}$ is the equivalent stress. More detailed

descriptions about the equivalent stress can be seen in [Wu \(2017\)](#).

Another variationally non-consistent phase field method can be seen in [Zhang et al. \(2017\)](#). The driving term H/G_c in the evolution equation is decomposed into two parts: H_1/G_{cI} and H_2/G_{cII} with

$$H_1 = \max_{\tau \in [0, t]} \lambda \langle \text{tr}(\boldsymbol{\varepsilon}) \rangle_+^2 \quad (51)$$

and

$$H_2 = \max_{\tau \in [0, t]} \mu \text{tr}[\langle \boldsymbol{\varepsilon} \rangle_+^2] \quad (52)$$

[Zhang et al. \(2017\)](#) regarded the parameters G_{cI} and G_{cII} as the respective strain energy release rates due to mode I and mode II deformations at a crack tip. However, their definition cannot practically distinguish between the tension and shear fractures. The governing equations of [Zhang et al. \(2017\)](#) are express as follows

$$\begin{cases} \nabla \cdot \boldsymbol{\sigma} + \mathbf{b} = 0 \\ (1 - \phi) \left(\frac{H_1}{G_{cI}} + \frac{H_2}{G_{cII}} \right) - \frac{1}{4\epsilon} \phi + \epsilon \Delta \phi = 0 \end{cases} \quad (53)$$

2.7 Similarities and differences between gradient-damage and phase field methods

In mathematics, the damage-based gradient-damage method ([de Borst and Verhoosel 2016](#)) and the phase-field methods for fractures are similar and these two types of methods have almost the same structures. Therefore, the difference between gradient-damage models and phase-field models is mainly in their interpretation and the interior length scale. Both damage-based gradient-damage and phase field methods introduce an intrinsic length scale into the discretization to smear the fracture over a localization band of finite width ([Zhou et al. 2018c](#)). However, in more detail, gradient-damage models used a spatial averaging operator and a local damage concept, whereas the phase field models follow the regularized energy variation due to fracture evolution and use a thermodynamic driving force for the smeared fracture. In addition, the vanishing derivative of the degradation function in the phase field ensures that the crack cannot broaden once the crack forms. Another difference is that crack broadening can be not predicted by the gradient-damage models ([de Borst and Verhoosel 2016](#)).

3 PFMs coupled with different discretization methods

3.1 Finite element method

Most of the phase field methods are solved within the framework of the finite element methods (FEM) because the governing equations in the phase field models are commonly seen partial difference equations that can be solved for by using FEM. The space domain can be easily discretized by finite elements and suitable decoupling technology can be used to solve the fully coupled phase field fracture problems. Some FE implementations of the phase field models of fracture can be seen in [Amor et al. \(2009\)](#); [Bourdin et al. \(2012\)](#); [Ehlers and Luo \(2017\)](#); [Heister et al. \(2015\)](#); [Hesch and Weinberg \(2014\)](#); [Kuhn and Müller \(2008\)](#); [Lee et al. \(2016\)](#); [Liu et al. \(2016\)](#); [Miehe et al. \(2010a\)](#); [Miehe and Mauthe \(2016\)](#); [Miehe et al. \(2015b, 2010b\)](#); [Mikelić et al. \(2015a,b\)](#); [Santillán et al. \(2017\)](#); [Sargado et al. \(2017\)](#); [Wheeler et al. \(2014\)](#); [Wick et al. \(2016\)](#); [Wu \(2017\)](#); [Yoshioka and Bourdin \(2016\)](#); [Zhou et al. \(2018a,c,d\)](#). In the following section, more details about the implementation by using the finite element methods will be demonstrated.

Although FEM has good capacity of implementing the phase field models, it is still difficult to solve high-order phase field equations by FEM. Therefore, some researchers tried to couple the phase field methods with other discretization technologies such as the isogeometric analysis and meshfree technology. More details about the isogeometric and meshfree methods will be presented in the following two subsections.

3.2 Isogeometric method

[Borden et al. \(2014\)](#) proposed a fourth-order model for the phase-field approximation of the variational formulation for brittle fracture. Based on energy balance, thermodynamically consistent governing equations are derived for the fourth-order phase-field model by using the variational fracture approach. The higher-order model has higher regularity in solving for the exact phase field. To implement the higher-order model, [Borden et al. \(2014\)](#) employed the isogeometric analysis framework and the smooth spline function spaces are used. The proposed higher-order model improves the convergence rate of the numerical solution and complex 3D crack propagation can be captured by the model of [Borden et al. \(2014\)](#).

The modified energy functional in the model of [Borden et al. \(2014\)](#) is expressed as

$$E(\mathbf{u}, s) = \int_{\Omega} ((s^2 + \eta)\Psi_0^+(\boldsymbol{\varepsilon}) + \Psi_0^-(\boldsymbol{\varepsilon})) \, d\Omega + G_c \int_{\Omega} \left[\frac{1}{4\epsilon}(1-s)^2 + \frac{1}{2}\epsilon|\nabla s|^2 + \frac{1}{4}\epsilon^3(\Delta s)^2 \right] \, d\Omega \quad (54)$$

By replacing Ψ_0^+ by the history field H , the resulting evolution equation of the higher-order

phase field model is

$$\frac{4\epsilon s H}{G_c} + s - 2\epsilon^2 \Delta s + \epsilon^4 \Delta(\Delta s) = 0 \quad (55)$$

Schillinger et al. (2015) tried to use the isogeometric collocation methods for the discretization of the second-order and fourth-order phase-field fracture models. The used isogeometric collocation methods are shown to speed up the phase-field fracture computations over general isogeometric Galerkin method because point evaluations are reduced. In addition, a hybrid collocation-Galerkin formulation is recommended by Schillinger et al. (2015) because it provides consistent weakly enforcing Neumann boundary conditions and multi-patch interface constraints. The hybrid collocation-Galerkin formulation can also deal with multiple boundary integral terms that arise from the weighted residual formulation and improve the phase field resolution (Schillinger et al. 2015).

Ambati and De Lorenzis (2016) applied a phase field model to investigate fracture in shells. The shell is modeled based on solid-shell kinematics with small rotations and displacements. The displacement and phase fields are discretized by using quadratic Non-Uniform Rational B-Spline basis functions. Goswami et al. (2020b) proposed a fourth-order phase field method with cubic-stress degradation function. Hybrid-staggered approach is used to solve the model, and PHT-splines are used to implement the adaptive refinement.

3.3 Meshfree method

Amiri et al. (2016) applied a fourth order phase-field model for fracture based on local maximum entropy (LME) approximants. Fourth order phase-field equations can be directly solved without splitting the fourth order differential equation into two second order differential equations due to the higher order continuity of the meshfree LME approximants.

The higher order crack surface density function used in Amiri et al. (2016) is identical to that in Borden et al. (2014). The meshfree discretization form of the displacement $\mathbf{u}(\mathbf{x})$ and phase field $s(\mathbf{x})$ is shown as follows,

$$\begin{cases} \mathbf{u}(\mathbf{x}) = \sum_a p_a \mathbf{u}_a \\ s(\mathbf{x}) = \sum_a p_a s_a \end{cases} \quad (56)$$

where p_a are LME basis functions, and u_a and s_a are nodal values of the displacement and phase fields. The same discretization is used on virtual displacements and virtual phase field parameters. In addition, the LME basis functions are non-negative and must satisfy the C^0 and C^1 consistency:

$$p(\mathbf{x}) \geq 0 \quad (57)$$

$$\sum_{a=1}^N p_a(\mathbf{x}) = 1 \quad (58)$$

$$\sum_{a=1}^N p_a(\mathbf{x}) \mathbf{x}_a = \mathbf{x} \quad (59)$$

where the vector \mathbf{x}_a denotes the positions of the nodes associated with each basis function. [Amiri et al. \(2016\)](#) used the local maximum entropy basis functions as follows,

$$p_a(\mathbf{x}) = \frac{1}{Z(\mathbf{x}, \boldsymbol{\lambda}^*(\mathbf{x}))} \exp[-\beta_a |\mathbf{x} - \mathbf{x}_a|^2 + \boldsymbol{\lambda}^*(\mathbf{x} - \mathbf{x}^*)] \quad (60)$$

where

$$Z(\mathbf{x}, \boldsymbol{\lambda}(\mathbf{x})) = \sum_{b=1}^N \exp[-\beta_b |\mathbf{x} - \mathbf{x}_b|^2 + \boldsymbol{\lambda}(\mathbf{x} - \mathbf{x}_b)] \quad (61)$$

is a function associated with a set of nodes $X = \{\mathbf{x}_a\}_{a=1, \dots, N}$ and $\boldsymbol{\lambda}^*$ is defined by

$$\boldsymbol{\lambda}^* = \arg \min_{\boldsymbol{\lambda} \in \mathbb{R}^d} \log Z(\mathbf{x}, \boldsymbol{\lambda}) \quad (62)$$

with d the dimension of the crack problem. The discrete stiffness and force matrices are then obtained by using the meshfree discretization to solve the crack problems. Note that the crack can propagate, branch and merge but cannot be recovered because a strong constraint $s_i \leq s_{i-1}$ is imposed with s_i and s_{i-1} are the phase fields at step i and $i - 1$.

3.4 Physics informed neural network

[Goswami et al. \(2020a\)](#) proposed the first physics informed neural network for phase field modeling of fracture. It seems that the PINN model treats the fracture problems one level higher on the model hierarchy than FEM. The proposed machine learning method is easy to implement and only a few lines of code are required. The approach can have a good computational savings compared with FEM after the network being trained.

3.5 FFT solver for phase field modeling

[Chen et al. \(2019\)](#) introduced an FFT algorithm to solve the phase-field model of brittle fracture. By using a staggered update scheme, the FFT algorithm solves the fracture and mechanical problems separately. The proposed method inherits the advantages of classical FFT methods in terms of simplicity of mesh generation and parallel implementation. In addition, [Ma and Sun \(2020\)](#) proposed an FFT-based solver for higher-order and multi-phase-field fracture, while the model was applied to strongly anisotropic brittle materials.

4 Finite element implementation of phase field methods

In this section, more details about the FE implementation of the phase field models are presented.

4.1 FE approximation

To show better of the FE approximation, we start from the governing equations in [Zhou et al. \(2018a\)](#) for example:

$$\begin{cases} \frac{\partial \sigma_{ij}}{\partial x_j} + b_i = \rho \ddot{u}_i \\ \left[\frac{2l_0(1-k)H}{G_c} + 1 \right] \phi - l_0^2 \frac{\partial^2 \phi}{\partial x_i^2} = \frac{2l_0(1-k)H}{G_c} \end{cases} \quad (63)$$

Note that these governing equations are used for dynamic problems. For quasi-static problems, the initial term vanishes. The weak form of the governing equations are subsequently given by

$$\int_{\Omega} (-\rho \ddot{\mathbf{u}} \cdot \delta \mathbf{u} - \boldsymbol{\sigma} : \delta \boldsymbol{\varepsilon}) d\Omega + \int_{\Omega} \mathbf{b} \cdot \delta \mathbf{u} d\Omega + \int_{\Omega_h} \mathbf{f} \cdot \delta \mathbf{u} dS = 0 \quad (64)$$

and

$$\int_{\Omega} -2(1-k)H(1-\phi)\delta\phi d\Omega + \int_{\Omega} G_c \left(l_0 \nabla \phi \cdot \nabla \delta\phi + \frac{1}{l_0} \phi \delta\phi \right) d\Omega = 0 \quad (65)$$

The standard vector-matrix notation is used and the discretization of the displacement and phase field can be expressed as

$$\mathbf{u} = \mathbf{N}_u \mathbf{d}, \quad \phi = \mathbf{N}_\phi \hat{\phi} \quad (66)$$

where \mathbf{u}_i and ϕ_i are the nodal values of the displacement and phase field. \mathbf{d} and $\hat{\phi}$ are the vectors consisting of node values \mathbf{u}_i and ϕ_i . \mathbf{N}_u and \mathbf{N}_ϕ are shape function matrices:

$$\mathbf{N}_u = \begin{bmatrix} N_1 & 0 & 0 & \dots & N_n & 0 & 0 \\ 0 & N_1 & 0 & \dots & 0 & N_n & 0 \\ 0 & 0 & N_1 & \dots & 0 & 0 & N_n \end{bmatrix}, \quad \mathbf{N}_\phi = \begin{bmatrix} N_1 & N_2 & \dots & N_n \end{bmatrix} \quad (67)$$

where n is the node number in one element and N_i is the corresponding shape function. The same discretization is assumed on the test functions:

$$\delta \mathbf{u} = \mathbf{N}_u \delta \mathbf{d}, \quad \delta \phi = \mathbf{N}_\phi \delta \hat{\phi} \quad (68)$$

where $\delta \mathbf{d}$ and $\delta \hat{\phi}$ are the vectors consisting of node values of the test functions.

These gradients are used:

$$\boldsymbol{\varepsilon} = \mathbf{B}_u \mathbf{d}, \quad \nabla \phi = \mathbf{B}_\phi \hat{\boldsymbol{\phi}}, \quad \delta \boldsymbol{\varepsilon} = \mathbf{B}_u \delta \mathbf{d}, \quad \nabla \phi = \mathbf{B}_\phi \delta \hat{\boldsymbol{\phi}} \quad (69)$$

where \mathbf{B}_u and \mathbf{B}_ϕ are the derivatives of the shape functions defined by

$$\mathbf{B}_u = \begin{bmatrix} N_{1,x} & 0 & 0 & \dots & N_{n,x} & 0 & 0 \\ 0 & N_{1,y} & 0 & \dots & 0 & N_{n,y} & 0 \\ 0 & 0 & N_{1,z} & \dots & 0 & 0 & N_{n,z} \\ N_{1,y} & N_{1,x} & 0 & \dots & N_{n,y} & N_{n,x} & 0 \\ 0 & N_{1,z} & N_{1,y} & \dots & 0 & N_{n,z} & N_{n,y} \\ N_{1,z} & 0 & N_{1,x} & \dots & N_{n,z} & 0 & N_{n,x} \end{bmatrix}, \quad \mathbf{B}_\phi = \begin{bmatrix} N_{1,x} & N_{2,x} & \dots & N_{n,x} \\ N_{1,y} & N_{2,y} & \dots & N_{n,y} \\ N_{1,z} & N_{2,z} & \dots & N_{n,z} \end{bmatrix} \quad (70)$$

The equations of weak form (64) and (65) are subsequently written as

$$-(\delta \mathbf{d})^T \left[\int_{\Omega} \rho \mathbf{N}_u^T \mathbf{N}_u d\Omega \ddot{\mathbf{d}} + \int_{\Omega} \mathbf{B}_u^T \mathbf{D}_e \mathbf{B}_u d\Omega \mathbf{d} \right] + (\delta \mathbf{d})^T \left[\int_{\Omega} \mathbf{N}_u^T \mathbf{b} d\Omega + \int_{\Omega_h} \mathbf{N}_u^T \mathbf{f} dS \right] = 0 \quad (71)$$

$$-(\delta \hat{\boldsymbol{\phi}})^T \int_{\Omega} \left\{ \mathbf{B}_\phi^T G_c l_0 \mathbf{B}_\phi + \mathbf{N}_\phi^T \left[\frac{G_c}{l_0} + 2(1-k)H \right] \mathbf{N}_\phi \right\} d\Omega \hat{\boldsymbol{\phi}} + (\delta \hat{\boldsymbol{\phi}})^T \int_{\Omega} 2(1-k)H \mathbf{N}_\phi^T d\Omega = 0 \quad (72)$$

Because of admissible arbitrary test functions, Eqs. (71) and (72) results in the discretized weak form equations:

$$-\underbrace{\int_{\Omega} \rho \mathbf{N}_u^T \mathbf{N}_u d\Omega \ddot{\mathbf{d}}}_{\mathbf{F}_u^{ine} = \mathbf{M} \ddot{\mathbf{d}}} - \underbrace{\int_{\Omega} \mathbf{B}_u^T \mathbf{D}_e \mathbf{B}_u d\Omega \mathbf{d}}_{\mathbf{F}_u^{int} = \mathbf{K}_u \mathbf{d}} + \underbrace{\int_{\Omega} \mathbf{N}_u^T \mathbf{b} d\Omega + \int_{\Omega_h} \mathbf{N}_u^T \mathbf{f} dS}_{\mathbf{F}_u^{ext}} = 0 \quad (73)$$

$$-\underbrace{\int_{\Omega} \left\{ \mathbf{B}_\phi^T G_c l_0 \mathbf{B}_\phi + \mathbf{N}_\phi^T \left[\frac{G_c}{l_0} + 2(1-k)H \right] \mathbf{N}_\phi \right\} d\Omega \hat{\boldsymbol{\phi}}}_{\mathbf{F}_\phi^{int} = \mathbf{K}_\phi \hat{\boldsymbol{\phi}}} + \underbrace{\int_{\Omega} 2(1-k)H \mathbf{N}_\phi^T d\Omega}_{\mathbf{F}_\phi^{ext}} = 0 \quad (74)$$

where \mathbf{F}_u^{ine} , \mathbf{F}_u^{int} , and \mathbf{F}_u^{ext} are the inertial, internal, and external forces for the displacement field and \mathbf{F}_ϕ^{int} and \mathbf{F}_ϕ^{ext} are the internal and external force terms of the phase field (Zhou et al. 2018a). Additionally, the mass and stiffness matrices read

$$\begin{cases} \mathbf{M} = \int_{\Omega} \rho \mathbf{N}_u^T \mathbf{N}_u d\Omega \\ \mathbf{K}_u = \int_{\Omega} \mathbf{B}_u^T \mathbf{D}_e \mathbf{B}_u d\Omega \\ \mathbf{K}_\phi = \int_{\Omega} \left\{ \mathbf{B}_\phi^T G_c l_0 \mathbf{B}_\phi + \mathbf{N}_\phi^T \left[\frac{G_c}{l_0} + 2(1-k)H \right] \mathbf{N}_\phi \right\} d\Omega \end{cases} \quad (75)$$

4.2 Solution schemes

There are two basic approaches to solve the coupling discretized equations (73) and (74): monolithic and staggered schemes. In a monolithic scheme, the displacement and phase field are solved simultaneously. Whereas, the phase field and displacement are solved independently for a staggered scheme. At a given time step, the displacement is solved first at a fixed phase field. By using the updated displacement, the phase-field equation is subsequently solved.

4.2.1 Monolithic scheme

For a monolithic scheme, the implicit Hughes-Hibert-Taylor (HHT) time integration can be adopted in the dynamic calculations (see Liu et al. (2016)). According to our experience, other integration methods such as the implicit BDF (backward differentiation formulas) and the generalized- α methods can also be successfully used in phase field modeling. As an example, the implicit HHT method is presented herein. Letting i be the Newton iteration, the residual force vectors now are re-written as (Liu et al. 2016):

$$(\mathbf{R}^u)_i^{t+\Delta t} = (\mathbf{F}_u^{ext})_i^{t+\Delta t} - (\mathbf{F}_u^{ine})_i^{t+\Delta t} - (1 + \alpha)(\mathbf{F}_u^{int})_i^{t+\Delta t} + \alpha(\mathbf{F}_u^{int})_i^t \quad (76)$$

$$(\mathbf{R}^\phi)_i^{t+\Delta t} = (\mathbf{F}_\phi^{ext})_i^{t+\Delta t} - (1 + \alpha)(\mathbf{F}_\phi^{int})_i^{t+\Delta t} + \alpha(\mathbf{F}_\phi^{int})_i^t \quad (77)$$

where $\alpha \in [\frac{1}{3}, 0]$ is the HHT integration operator and $\Delta t = t_{n+1} - t_n$ is the time step size. If the material damping effect is neglected, the tangent matrix in one element is given by (Liu et al. 2016):

$$\mathbf{S}_{ij} = \mathbf{M}_{ij} \frac{d\ddot{\mathbf{u}}}{d\mathbf{u}} + (1 + \alpha)\mathbf{K}_{ij} \quad (78)$$

$$\frac{d\ddot{\mathbf{u}}}{d\mathbf{u}} = \frac{1}{\beta\Delta t^2}, \quad \beta = \frac{(1 - \alpha)^2}{4} \quad (79)$$

4.2.2 Staggered scheme

In a staggered scheme, greater flexibility exists in solving the displacement and phase field. This means both implicit and explicit time schemes can be used. In an implicit approach, the procedure of solving displacement field is similar to those in a monolithic scheme. Whereas for an explicit method, e.g. the explicit central-difference time-integration method, some modification is needed (Liu et al. 2016):

$$(\mathbf{u})_i^{t+\Delta t} = (\mathbf{u})_i^t + (\dot{\mathbf{u}})_i^{t+0.5\Delta t} \Delta t \quad (80)$$

$$(\dot{\mathbf{u}})_i^{t+0.5\Delta t} = (\dot{\mathbf{u}})_i^{t-0.5\Delta t} + (\ddot{\mathbf{u}})_i^t \Delta t \quad (81)$$

and

$$(\ddot{\mathbf{u}})_i = (\mathbf{M}_{ij})^{-1} ((\mathbf{F}_u^{ext})_i - (\mathbf{F}_u^{int})_i) \quad (82)$$

Seleš et al. (2019) discussed the details of a residual control staggered solution scheme for the phase-field modeling of brittle fracture. The use of a stopping criterion within the broadly used staggered algorithm was discussed. The methods of stopping criterion of the iterative scheme are based on the residual norm and implemented in commercial software ABAQUS. The proposed method can avoid fine loading incrementation to produce an accurate solution in a common single iteration staggered algorithm.

4.3 Implementation codes

To reduce the implementation effort on the phase field methods and facilitate new learners, some phase field models are developed and implemented with commonly used commercial software. Commonly seen are the Abaqus, FEniCS and COMSOL implementations.

4.3.1 Abaqus implementation

Liu et al. (2016); Msekhi et al. (2015) implement the isotropic and anisotropic types of phase field methods in Abaqus. For the monolithic scheme, a UEL subroutine is used. The time integration and element discretization are implemented in the Abaqus standard and the UEL subroutine calls for each iteration in a given increment. Because Abaqus itself does not support a plot of the results on the used elements, external visualization software is required for better exporting the calculated results (Liu et al. 2016).

For a staggered scheme, a UMAT or VUMAT subroutine is used. If an implicit time integration scheme is used, a UMAT subroutine is employed to exchange the local history field H and the phase field ϕ on integration points. Subsequently, the stress σ and its tangent modulus with ε must be renewed in every iteration. Whereas, if an explicit time integration scheme is used, a VUMAT subroutine is employed to exchange the local history field H and the phase field ϕ instead, and only the stress σ needs to be renewed during each increment.

Zhang et al. (2018) implemented an iterative scheme in Abaqus for cohesive fractures. Fang et al. (2019) presented Abaqus implementation procedures of phase field fracture of elasto-plastic solids in a staggered manner. The subroutines UEL and UMAT are also used. The UMAT describes the constitutive behavior of elasto-plastic solids, while the UEL is designed for the phase field fracture. The authors solved the phase field and displacement field separately using the Newton-Raphson iteration method.

4.3.2 COMSOL implementation

Zhou et al. (2018a,c,d) implemented the anisotropic type of phase field models in the multi-field simulator—COMSOL Multiphysics. The implementations in COMSOL are much easier to be extended to problems with more fields than other software such as Abaqus. The modules

established in COMSOL is shown in Fig. 2 and the implementation procedure in COMSOL is shown in Fig. 3.

As shown in Fig. 2, the “Storage Module” stores the results obtained from the “Solid Mechanics Module”, such as the principal strains and their directions. The positive part of the elastic energy is then calculated to update the local history strain field. Subsequently, the updated history strain is used to solve the phase-field. Because of the highly nonlinearity, the elasticity matrix in the “Solid Mechanics Module” must be modified by the updated phase-field solution and varying principal strains and their corresponding directions. Note that only staggered schemes are used in Zhou et al. (2018a,c,d). In addition, the implicit Generalized- α method is used for time integration. For convergence issues, Anderson acceleration technology is used to increase the convergence rate in COMSOL and the open-access codes of the phase field modeling in COMSOL can be found in “<https://sourceforge.net/projects/phasefieldmodelingcomsol/>”.

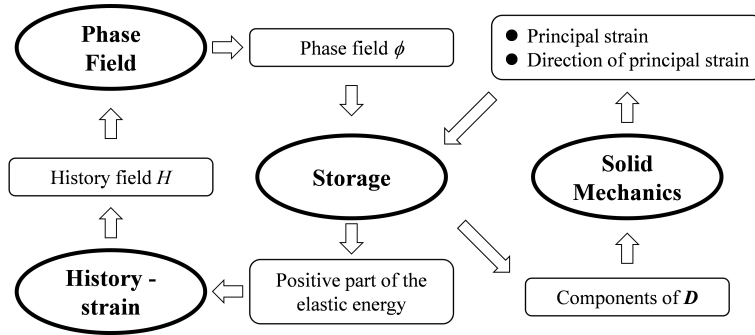


Fig. 2 Established modules in COMSOL for the phase field modeling

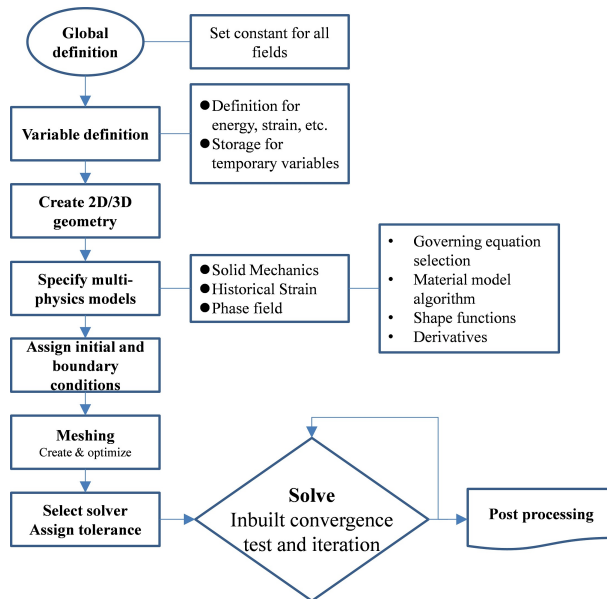


Fig. 3 Implementation procedure in COMSOL for the phase field modeling (Zhou et al. 2018a)

4.3.3 FEniCS implementation

Natarajan et al. (2019) presented a FEniCS implementation scheme of the phase field method for quasi-static brittle fracture. The FEniCS provides a framework for the automated solutions of the partial differential equations. Therefore, the phase field and displacement field can be solved, respectively. However, in recent days, the performance of FEniCS implementation has not been verified in comparison with Abaqus and COMSOL implementations.

4.4 Computational cost

To obtain accurate results predicted from the phase field models of fracture, it is heavily time-costing even in 2D problems when the finite element method is used. One reason is that the resolution of the small length-scale requires extremely fine meshes, at least near the region with high phase field ϕ . That is, if no adaptive mesh refinement technology is used, the phase field models are calculated on fine fixed meshes, which requires high computational cost. Another reason is that energy split technology is used to obtain realistic crack patterns under tension and compression. The special split such as the strain decomposition (Miehe et al. 2010a) results in a highly non-linear constitutive model of stress to strain. Rather many iterations are needed to solve the highly non-linear constitutive model. In addition, to obtain a better crack resolution, the loading and displacement increments must be small enough. Too small increments make the computational cost expensive even for a simple isotropic phase field model.

4.5 Element technologies

The phase field methods are in general laborious approaches to fracture and thereby some element technologies are developed to improve the efficiency of the phase field methods within the framework of FEM.

4.5.1 Adaptive mesh refinement

To develop a robust and efficient numerical scheme for the phase field modeling, a primal-dual active set method and predictor-corrector mesh adaptivity technology were used in Heister et al. (2015). The primal-dual active set method is a semi-smooth Newton method, which maintains the crack irreversibility as a constraint and achieved increasing converging rate. The predictor-corrector mesh adaptivity technology is also developed by Heister et al. (2015) to reduce the computational cost. This adaptive mesh refinement technology has following features:

- Keep a single fixed, small strain ϵ during the entire computation.
- Ensure $h < \epsilon$ inside crack region.
- Error is controlled by ϵ , not the element size h .

- No requirement of prior knowledge about crack paths.
- Handling fast growing cracks.

Wick (2016) developed a posteriori error estimation and goal-oriented adaptive mesh refinement technology for phase field crack propagation. Goal functionals and dual-weighted residual (DWR) methods are used simultaneously. Their approach is based on a partition-of-unity (PU) and does not require strong residuals nor jumps over element edges.

In addition, Badnava et al. (2018); Zhou and Zhuang (2018) used another adaptive mesh refinement method to couple the phase field method (so-called h-adaptive phase field method). The adaptive mesh refinement does not require the mesh refinement around a pre-fixed crack path. Instead, a predictor-corrector scheme for mesh adaptivity is used. First, the coupled system with coarser elements is solved and predicts an initial crack path. Subsequently, a refinement threshold such as $\phi > 0.85$ is used to judge if the mesh requires refinement. Finally, all the fields are solved again based on the refined mesh (Zhou and Zhuang 2018). The predictor-corrector mesh refinement is continuously imposed on the elements in one time step unless the elements do not need refinement. Tian et al. (2019) proposed a novel hybrid adaptive finite element phasefield method (haPFM) for fractures under quasistatic and dynamic loading. The method refines adaptively the meshes based on a crack tip identification strategy while the refined meshes in the noncrack progression region are reset as coarse meshes. The proposed method prominently reduces the CPU time and memory usage. Jansari et al. (2019) used a recovery based error indicator and quadtree decomposition to establish an adaptive phase field method for quasi-static brittle fracture. Kristensen and Martínez-Pañeda (2020) investigated the potential of quasi-Newton methods in facilitating convergence of monolithic solution schemes for phase field modelling. A new adaptive time increment scheme is proposed to reduce the computational cost. The study indicates computation times can be reduced by several orders of magnitude. On the other hand, the number of load increments required by the staggered solution will be up to 3000 times higher. Noii et al. (2020) proposed an adaptive global–local approach for phase-field modeling of anisotropic brittle fracture.

4.5.2 Multi-scale phase field method

Patil et al. (2018) coupled a multi-scale finite element method (MsFEM) with the hybrid type of phase field model for brittle fracture problems. This multi-scale method is also coupled with adaptive remeshing technology and named the adaptive multi-scale phase field method (AMPFM). An important feature of this phase field method is that the degrees of freedom of coarse-mesh and fine-mesh are linked together using multi-scale basis functions during mesh refinement (Patil et al. 2018). The crack propagation path is automatically tracked and refined around the crack by using the current phase field and its increment. Another benefit of AMPFM

is that memory and CPU time are dramatically reduced when AMPFM is used to simulate the brittle fracture in heterogeneous structures with uniformly distributed small-size discontinuities. [Gerasimov et al. \(2018\)](#) adopted non-intrusive global/local approaches when the fracture was modeled by using the phase-field framework.

4.5.3 New element shape function

In another effort to reduce computational cost of the phase field, [Kuhn and Müller \(2011\)](#) developed special engineered FEM shape functions to discretize the phase field. The shape functions have an exponential nature and their forms are as follows,

$$N_1^e(\xi, \delta) = 1 - \frac{\exp(-\delta(1 + \xi)/4) - 1}{\exp(\delta/2) - 1} \quad (83)$$

$$N_2^e(\xi, \delta) = \frac{\exp(-\delta(1 + \xi)/4) - 1}{\exp(\delta/2) - 1} \quad (84)$$

where δ is the ration between the element size and the scale parameter of the phase field method.

Note that Eqs. (83) and (84) are only available in 1D 2-node element. For 2D, the shape functions for a 4-node element are obtained as the tensor products of the above Eqs. (83) and (84) with some changes. The results of [Kuhn and Müller \(2011\)](#) showed that accurate prediction of the surface energy can be achieved in a much lower element refinement level by using the special shape functions. A drawback of the approach of [Kuhn and Müller \(2011\)](#) is that some prior information about the fracture direction is needed to construct the exponential shape functions.

4.5.4 Virtual element and smooth finite element

[Aldakheel et al. \(2018\)](#) proposed an efficient low order virtual element scheme for phase-field modeling of brittle fracture. The virtual element formulation has flexible choice of node number in an element that can be changed in a simulation. The potential density is written in terms of polynomial functions rather than the unknown shape functions for complicated element geometries. [Bhowmick and Liu \(2018\)](#) developed a phase field model in the framework of cell-based smoothed finite element method (CS-FEM). The CS-FEM is softer than the standard FEM, and CS-FEM is used to solve the equations that govern the continuum mechanics of solids. The computational cost of CS-FEM is slightly lower than the finite element counterpart.

4.6 Special treatments

4.6.1 Modelling pre-existing cracks

How to model pre-existing cracks is another important issue in phase field modelling. A straightforward manner is to model initial cracks as discrete cracks using double nodes in the element mesh. However, the phase field can also be used to model the initial pre-existing cracks. The first way is to constrain the phase field by the Dirichlet boundary condition $\phi = 1$ at the pre-existing crack. The nodes with $\phi = 1$ can be placed on a single line or a small region. But the latter produces larger error on calculating the crack surface energy. Another way to model pre-existing crack is the approach proposed by [Borden et al. \(2012\)](#) where an initial history energy field is introduced. The history field has the following form:

$$H_0(\mathbf{x}) = B \begin{cases} \frac{G_c}{4\epsilon} \left(1 - \frac{d(\mathbf{x}, l)}{\epsilon}\right) & d(\mathbf{x}, l) \leq \epsilon \\ 0 & d(\mathbf{x}, l) > \epsilon \end{cases} \quad (85)$$

where $B = 1 \times 10^3$ and $d(\mathbf{x}, l)$ is the closest distance from \mathbf{x} to the line l .

4.6.2 Determining crack tip position

Because the phase field method applies diffusive description of the sharp crack, there is no obvious sharp crack tip in the modelling. But for post-processing, the crack tip position is sometimes needed especially when the crack velocity and accumulated crack length are calculated. For 2D problems, the crack tip is commonly defined by using the iso-curves of the phase-field ([Borden et al. 2012](#); [Liu et al. 2016](#); [Zhou et al. 2018a](#)). For example, [Borden et al. \(2012\)](#) used the iso-curves of $\phi = 0.75$ to fix the crack tip position. In addition, [Nguyena and Wub](#) adopted another approach. They selected all nodes that have a phase field larger than 0.8, while the crack tip is fixed on the node that has the maximum horizontal coordinate among those selected nodes.

4.6.3 Hierarchical meshes

[Goswami et al. \(2019\)](#) proposed a novel dual-mesh based adaptive phase field method for solving fracture problems. The implementation of the phase field model is based two sets of meshes with different characteristic element sizes. A coarser mesh for the displacement field and a finer mesh is for the phase field. To facilitate the exchange of information between the meshes, the authors also proposed an efficient data transfer algorithm.

5 Extensions and applications of the PFMs

5.1 Ductile fracture

Extensions of the phase field methods to ductile fractures are exclusively based on the variational approach to fracture. These extensions are mostly based on the coupling of phase field methods with models of elasto-plasticity (Miehe et al. 2016). Duda et al. (2015) examined a series of brittle fractures in elastic-plastic solids. Other variational approaches of modelling combined brittle-ductile fractures can be seen in Alessi et al. (2015); Ulmer et al. (2013). The model of Ambati et al. (2015a) suggested a characteristic degradation function. By using this function, the damage is coupled to plasticity in a multiplicative format (Miehe et al. 2016). However, combination of the local plasticity models and the gradient-damage-type phase field modeling of fracture in Ambati et al. (2015a) do not meet the constraints on the plastic and damage length scales (Miehe et al. 2016). The model of Ambati et al. (2015a) also lacks a canonical structure based on variational principles. This drawback is overcome by the following work of Miehe et al. (2015a), which couples gradient plasticity to gradient damage at finite strains.

Miehe et al. (2016) proposed a consistent variational framework for the phase field modelling of ductile fractures in elastic-plastic solids at large strains. The bases of the model in Miehe et al. (2016) are the formulation of variational gradient plasticity in Miehe et al. (2014) and the original phase field model for brittle fractures in Miehe et al. (2010a,b). Ambati and De Lorenzis (2016) applied a phase field model to investigate fracture in shells. The solid-shell formulation is distinguished between elastic and plastic materials. A brittle phase-field model is used for elastic materials, while a ductile fracture model for elasto-plastic materials with J_2 plasticity and isotropic hardening.

In Ambati and De Lorenzis (2016), the total free energy functional E_l for the ductile fracture is the sum of elastic, plastic, and fracture energy contributions:

$$E_l(\boldsymbol{\varepsilon}_e, \boldsymbol{\varepsilon}_p, h, s) = \int_{\Omega} [g(s, p)\Psi_e^+(\boldsymbol{\varepsilon}) + \Psi_e^-(\boldsymbol{\varepsilon}) + \Psi_p(h) + \gamma(s, \nabla s)] \, d\Omega \quad (86)$$

where $\Psi_p(h)$ is the plastic strain energy density function with isotropic hardening variable h . $\boldsymbol{\varepsilon}_e$ and $\boldsymbol{\varepsilon}_p$ are the respective elastic and the plastic strain tensors with the total strain $\boldsymbol{\varepsilon} = \boldsymbol{\varepsilon}_e + \boldsymbol{\varepsilon}_p$. The similar decomposition of the energy to Eq. (17) is used

$$\begin{cases} \Psi_e^+(\boldsymbol{\varepsilon}) = \frac{1}{2}K_n \langle \text{tr}(\boldsymbol{\varepsilon}) \rangle_+^2 + \mu(\boldsymbol{\varepsilon}^D : \boldsymbol{\varepsilon}^D) \\ \Psi_e^-(\boldsymbol{\varepsilon}) = \frac{1}{2}K_n \langle \text{tr}(\boldsymbol{\varepsilon}) \rangle_-^2 \end{cases} \quad (87)$$

where $K_n = \lambda + 2/3\mu$ is the bulk modulus of the material.

The stress degradation function $g(s, p)$ is chosen as follows:

$$g(s, p) = s^{2p^m} + \eta \quad (88)$$

where m and p are two parameters with

$$p = \frac{\varepsilon_p^{eq}}{\varepsilon_{p,crit}^{eq}}, \quad \varepsilon_p^{eq}(t) = \sqrt{\frac{2}{3}} \int_0^t \sqrt{\dot{\boldsymbol{\varepsilon}}_p : \dot{\boldsymbol{\varepsilon}}_p} \quad (89)$$

and $\varepsilon_{p,crit}^{eq}$ is a threshold value, and ε_p^{eq} is the von Mises equivalent plastic strain.

In addition, [Borden et al. \(2016\)](#) presented a phase field formulation for fractures in ductile materials. They introduced a cubic degradation function, which produces a more accurate stress-strain response prior to crack initiation. A microforce-driven governing equation is used to replace the general energy potential for finite deformation problems. [Borden et al. \(2016\)](#) also introduced a yield surface degradation function that accounts for plastic softening and non-physical elastic deformations after crack initiation.

[Shanthraj et al. \(2016\)](#) applied a obstacle phase field energy model to formulate the fracture behavior in a finite strain elasto-viscoplastic material. The obstacle energy model can produce physically realistic fracture behaviors at the vicinity of the crack tip. The resulting variational inequality is discretized by a finite element method, and is solved by using a reduced space Newton method. [Shanthraj et al. \(2016\)](#) also emphasized a significant decrease in the computational cost by using their method. [Alessi et al. \(2018\)](#) also proposed a phase field model for plasticity. Based on a minimization algorithm, the coupled elasto-damage-plasticity can be solved by using the proposed method. [Dittmann et al. \(2018\)](#) proposed a higher order phase-field model for non-linear ductile fracture problems. The approach can easily account for the entire range of ductile fracture in the framework of non-linear elastoplasticity. A novel multiplicative triple split of the deformation gradient and a novel critical fracture energy are involved in the proposed model.

5.2 Cohesive fracture

For cohesive fracture, [Verhoosel and de Borst \(2013\)](#) developed a phase field model for straight crack propagation and the numerical modeling is implemented within the framework of the finite element method. In addition to the displacement and phase field fields in a general phase field method for brittle fractures, an auxiliary field was used to represent the displacement jump across the crack. This third field is kept constant orthogonal to the crack. [Vignollet et al. \(2014\)](#) extended the work of [Verhoosel and de Borst \(2013\)](#) and an arc length method and staggered scheme were used. However, the model of [Vignollet et al. \(2014\)](#) requires a pre-defined path for the fracture propagation.

5.3 Dynamic fracture

Numerical modelling of dynamic fractures in solids based on sharp crack discontinuities (e.g. XFEM) is difficult in dealing with complex crack topologies and requires special branching criteria such as XFEM. The phase field based dynamic modelling can overcome these drawbacks. Following the static phase field model of [Miehe et al. \(2010a,b\)](#), [Hofacker and Miehe \(2012, 2013\)](#) proposed a computational framework of phase field modelling of diffusive dynamic fractures. The proposed modelling method allows complex crack patterns. The dynamic approach follows the history energy field introduced by [Miehe et al. \(2010a\)](#). This auxiliary field contains a maximum reference energy obtained in the deformation history and drives the diffusive crack evolution. In addition, [Hofacker and Miehe \(2012, 2013\)](#) applied the energy split scheme introduced in [Miehe et al. \(2010a\)](#). Some representative examples of complex crack patterns are also presented by [Hofacker and Miehe \(2012, 2013\)](#).

[Borden et al. \(2012\)](#) proposed a compact phase field description of dynamic fractures. The presented method is similar to that proposed by [Hofacker and Miehe \(2012, 2013\)](#). Both monolithic and staggered time integration schemes are presented by [Borden et al. \(2012\)](#). For the dynamic description, the kinetic energy Ψ_{kin} is considered:

$$\Psi_{kin}(\dot{\mathbf{u}}) = \frac{1}{2} \int_{\Omega} \rho \dot{u}_i \dot{u}_i d\Omega \quad (90)$$

where $\dot{\mathbf{u}} = \frac{\partial \mathbf{u}}{\partial t}$ and ρ is the mass density of the material.

The final energy functional is modified as

$$E = \int_{\Omega} \left\{ \frac{1}{2} \rho \dot{u}_i \dot{u}_i - \Psi_e - G_c \left[\frac{(1-s)^2}{4\epsilon} + \epsilon \frac{\partial s}{\partial x_i} \frac{\partial s}{\partial x_i} \right] \right\} d\Omega \quad (91)$$

with

$$\Psi_e = [(1-k)s^2 + k] \Psi_0^+ + \Psi_0^- \quad (92)$$

The resulting governing equations of the dynamic problem are expressed as follows,

$$\begin{cases} \nabla \cdot \boldsymbol{\sigma} = \rho \ddot{\mathbf{u}} \\ \left[\frac{4\epsilon(1-k)H}{G_c} + 1 \right] s - 4\epsilon^2 \Delta s = 1 \end{cases} \quad (93)$$

[Nguyen and Wu \(2018\)](#) extended the phase-field cohesive zone model for static fracture to dynamic fracture in brittle and quasi-brittle solids. The performance of the dynamic model is tested on several benchmarks for both dynamic and cohesive brittle fractures. [Geelen et al. \(2019\)](#) also extended the phase field formulation to dynamic cohesive fracture. The model is characterized by a regularized fracture energy that is linear in the phase field, as well as non-polynomial

degradation functions. The authors examined two categories of degradation functions. [Ren et al. \(2019\)](#) proposed an explicit phase field model for dynamic brittle fracture. The mechanical field is integrated with a Verlet-velocity scheme, and the phase field is incremented with sub-steps at each step. Adaptive sub-stepping is applied by using the phase field residual, and the explicit scheme avoids the numerical difficulty in convergence and the calculation of anisotropic stiffness tensor. In addition, the phase field modulus is used rather than conventional phase field viscosity.

5.4 Finite deformation fracture

The variational approach for brittle fracture such as the original regularized formulation of [Bourdin et al. \(2000\)](#) can be extended to the problems of finite deformation fracture. [Kuhn \(2013\)](#) modified the original phase field model to describe fractures in Neo-Hookean materials and the elastic energy density becomes:

$$\Psi_e = (s^2 + \eta) \left[\frac{\lambda}{4} (J^2 - 1) - \left(\frac{\lambda}{2} + \mu \right) \ln J + \frac{\mu}{2} (\text{tr}(\mathbf{C} - 3)) \right] \quad (94)$$

where J is the determinant of the deformation gradient, and \mathbf{C} is the right Cauchy-Green tensor. If the surface energy density $\gamma(s, \nabla s)$ is unaltered, the thermodynamical restriction yields the constitutive relation:

$$\mathbf{S} = 2 \frac{\partial \Psi_e}{\partial \mathbf{C}} = (s^2 + \eta) \left[\frac{\lambda}{2} (J^2 - 1) \mathbf{C}^{-1} + \mu (\mathbf{1} - \mathbf{C}^{-1}) \right] \quad (95)$$

where \mathbf{S} is the second Piola-Kirchhoff stress tensor, and $\mathbf{S} = \mathbf{F}^{-1} \mathbf{P}$ with \mathbf{P} being the first Piola-Kirchhoff stress tensor. Being constructed in the reference configuration, the balance equation of the phase field modelling reads

$$\nabla \cdot \mathbf{P} + \mathbf{f}_0 = \mathbf{0} \quad (96)$$

where \mathbf{f}_0 is the body force vector.

Finally, the modified evolution equation of the crack phase field is expressed as

$$-\frac{\dot{s}}{M} = s \left[\frac{\lambda}{2} (J^2 - 1) - (\lambda + 2\mu) \ln J + \mu \text{tr}(\mathbf{C}) - 3 \right] - G_c \left(2\epsilon \Delta s + \frac{1-s}{2\epsilon} \right) \quad (97)$$

Note that all the parameters used in Eq. (97) are consistent with those in the model of [Kuhn and Müller \(2008\)](#). [Hesch and Weinberg \(2014\)](#) established another phase-field method for finite deformations and general nonlinear materials. A multiplicative split of the principal stretches is used to account for the fracture behaviors under tension and compression. [Hesch and Weinberg \(2014\)](#) also used an energy-momentum consistent integrator and their phase field

model is thermodynamically consistent.

5.5 Anisotropic fracture

Anisotropy is inherent to crystalline materials (among others) due to the symmetry of the atomic lattice (Nguyen et al. 2017). Failure anisotropy seemingly conflicts with the local symmetry and maximum energy release rate used in commonly used phase field model such as the model of Miehe et al. (2010a,b); Zhou et al. (2019a). Therefore, Li et al. (2015) proposed a variational phase-field model for strongly anisotropic fracture. In their model, higher-order phase-field description is implemented in a direct Galerkin way with smooth local maximum entropy approximants.

Nguyen et al. (2017) proposed a phase field model that could simulate non-free anisotropic crack bifurcations in a robust and fast implementation framework. The key in the model of Nguyen et al. (2017) is an introduction of the new crack surface density function:

$$\gamma(\phi, \nabla\phi, \mathbf{w}) = \frac{1}{2l_0}\phi^2 + \frac{l_0}{2}\mathbf{w} : (\nabla\phi \otimes \nabla\phi) \quad (98)$$

where \mathbf{w} is a second-order structural tensor that characterizes the type of anisotropy and \mathbf{w} is an invariant with respect to rotations. \mathbf{w} can be expressed as follows,

$$\mathbf{w} = \mathbf{1} + \beta_2(1 - \mathbf{M} \otimes \mathbf{M}) \quad (99)$$

where \mathbf{M} is the unit vector normal to the preferential cleavage plane, and parameter $\beta_2 \geq 0$ is used to penalize the damage on planes not normal to \mathbf{M} . In the case of isotropic material, β_2 is naturally equal to 0.

Bryant and Sun (2018) proposed a mixed-mode phase field fracture model in anisotropic rocks with consistent kinematics. The mixed-mode driving force of the phase field is obtained by balancing the microforce. In the method, local fracture dissipation determines the crack propagation and kinematics modes. Pillai et al. (2020) proposed an anisotropic cohesive phase field model for quasi-brittle fractures in thin fibre-reinforced composites.

5.6 Plate and shell fractures

In this section, we provide an overview of phase field approaches applied to dimensionally reduced continua according to their complexity from linear to nonlinear regimes. Generally, phase field models applied in solid bodies can be applied to thin structures, however, the most difficulty is how to make quantities in phase field modeling consistent with ones in shell kinematics which are often described on local frames, i.e, curvilinear coordinates. On the other hand, what makes it different between published works until now is related to types of shell models, of phase field

models and of discretization methods used, which are summarized in Table 2. Here, we adopt the notion that classifies types of phase field model according to [Miehe et al. \(2010a\)](#), in which an approach that splits strain energy and stress tensor into negative and positive parts is regarded as anisotropic phase field model. While a model whose entire elastic energy is degraded in fracture zones is called isotropic, one that still keeps linear in the momentum balance equation but performs a decomposition on the elastic strain energy is referred as a hybrid phase field model [Ambati et al. \(2015b\)](#). We also note that details of related shell models are not emphasized in this section, instead, we refer to other review papers of shell models, see e.g [Bischoff et al. \(2018\)](#).

Table 2: Overview of phase field approaches in thin structures

Model name	Shell model	Phase field model	Discretization method
Ulmer et al. (2012)	Mindlin-Reissner	anisotropic	standard FEM
Amiri et al. (2014)	Kirchhoff-Love	isotropic	Local Maximum-Entropy meshfree method
Kiendl et al. (2016)	Kirchhoff-Love	anisotropic	NURBS-based isogeometric analysis
Ambati and De Lorenzis (2016)	Solid-shell	anisotropic	NURBS-based isogeometric analysis
Areias et al. (2016c)	Corotational shell	hybrid	standard FEM
Reinoso et al. (2017)	Solid-shell	isotropic	standard FEM

The first work that applied phase field model in plates and shells is proposed by [Ulmer et al. \(2012\)](#), in which the shell model is considered as a combination of standard plates and membranes, which allows them to use standard Lagrangian polynomials to approximate solution fields as the shell model only requires C0–continuity of basis functions. On the other hand, elastic energy is split into bending part and membrane part which further is divided into positive and negative components. Accordingly, full of bending energy and positive membrane energy contribute to fracture progression. The free energy functional of this approach takes the form of

$$E(\mathbf{u}, d) = \int_V [g(d)(\mathcal{E}_m^+(\boldsymbol{\varepsilon}_m) + \mathcal{E}_b(\boldsymbol{\kappa})) + \mathcal{E}_m^-(\boldsymbol{\varepsilon}_m) + \mathcal{F}(d, \nabla d)] dV, \quad (100)$$

where \mathcal{E}_m is the membrane energy, \mathcal{E}_b bending energy, $\mathcal{F}(d, \nabla d)$ fracture energy, and $g(d)$ the degradation function.

In 2014, [Amiri et al. \(2014\)](#) applied the isotropic phase field model to Kirchhoff -Love thin shell, for which they use Local Maximum-Entropy meshfree approximations to fulfill the requirement of C1–continuity of basis functions which arises from the appearance of second derivatives in the bending strain of the shell model. [Kiendl et al. \(2016\)](#) introduced an approach that combine the anisotropic phase field model with Kirchhoff-Love thin shell and NURBS basis functions are used to approximate solution fields. They also shown that the two mentioned works had some limitations as they may prevent crack propagation and be not realistic for fracture phenomenon at some circumstances. Amiri’s approach employs the isotropic model that makes it only applicable to cases of tensile stress states, while Ulmer’s model leads to delay of cracking

in cases of combination between bending and compressive membrane strains or may result in evolving damage under cases of purely compressive strains . Accordingly, Eq. 100 is rewritten as

$$E(\mathbf{u}, d) = \int_V [g(d)\mathcal{E}^+(\boldsymbol{\varepsilon}) + \mathcal{E}^-(\boldsymbol{\varepsilon}) + \mathcal{F}(d, \nabla d)]dV \quad (101)$$

where total strain $\boldsymbol{\varepsilon} = \boldsymbol{\varepsilon}_m + \theta^3 \boldsymbol{\kappa}$ with $\boldsymbol{\varepsilon}_m$ and $\boldsymbol{\kappa}$ as membrane strain and curvature change respectively. In Eq. 101, both membrane and bending strains contribute to total strain tensor which is split into tensile and membrane components, which prohibits the decomposition of elastic energy into membrane and bending terms . In contrast with the aforementioned works that employed the classical thin shell models, [Ambati and De Lorenzis \(2016\)](#) investigated the anisotropic phase field approach to a solid-shell element whose kinematics quantities are defined through the thickness instead of on the mid-surface as in the Kirchhoff-Love shell. The employed solid-shell formulation is rotation-free, which motivates inheriting the same nodes and degrees of freedom of the solid element, allowing to model fracture for elasto-plastic materials by using general three dimensional (3D) elasto-plastic constitutive models, i.e J2 plasticity, see e.g [Ambati et al. \(2015a\)](#) for ductile fracture model in solid.

One thing to note is that all the phase field models in thin structures above are formulated in linear regime, which makes them very limited , since in reality shell structures are usually undergone large deformation and rotation. To overcome this, [Areias et al. \(2016c\)](#) developed a hybrid phase field approach to the so-called corotational shell at finite strain. Kiendl's work ([Kiendl et al. 2016](#)) which ensures the irreversibility of crack evolution in the case of elasto-plasticity by the local history field which is the maximum of the positive elastic energy obtained within each loading step, Areias's model suggests another criteria for the irreversibility of crack phase field as

$$\mathcal{H} = \langle \max(W_p - W_p^*) \rangle_+ \quad (102)$$

with W_p as the plastic work and W_p^* as the critical value of the plastic work, which enables to employ the work of separation in the ductile fracture ([Siegmund and Brocks 2000](#)). Furthermore, to get consistent in the extension of infinitesimal-strain regime for the continuum phase field model to the case of the employed finite strain shell, a consistent updated-Lagrangian algorithm, where a reference configuration is not chosen as the undeformed configuration, is adopted, see [Areias et al. \(2016c\)](#) for details. Recently, [Reinoso et al. \(2017\)](#) introduced an approach combining the isotropic phase field model with a six-parameter solid-shell element which consists of three displacements on the mid-surface, two independent rotations and additional degree of freedom accounting for thickness stretch. Large deformation as well as linear and nonlinear elastic constitutive laws are considered in this work. Note that, both Areias' and Reinoso's models describe variations of phase field through the shell thickness that leads to a correct description of fracture

in bending-dominated cases. This is in contrast with previous works that assume invariance of the phase field variable over the shell thickness. Following [Areias et al. \(2016c\)](#), phase field is linearly interpolated between top and bottom faces of the shell as follows

$$d(\theta^1, \theta^2, \theta^3) = \frac{1}{2}(1 + \theta^3)d_{top}(\theta^1, \theta^2) + \frac{1}{2}(1 - \theta^3)d_{bottom}(\theta^1, \theta^2) \quad (103)$$

where d_{top} and d_{bottom} are phase field variables at top and bottom faces respectively, while θ^1 , θ^2 and θ^3 are coordinates in the parametric space with (θ^1, θ^2) as the in-plane directions and θ^3 as the thickness direction.

5.7 Thermal fracture

The phase field approach can be used for thermal fracture modelling. To study thermally induced fractures, the thermal strains are required in the total energy functional. At small strains, the total strain is the sum of elastic and thermal strains. With a thermal expansion tensor $\boldsymbol{\alpha}$, the thermal strain is $\boldsymbol{\varepsilon}^\theta = \theta\boldsymbol{\alpha}$, and the total strain $\boldsymbol{\varepsilon}$ reads

$$\boldsymbol{\varepsilon} = \boldsymbol{\varepsilon}^e + \boldsymbol{\varepsilon}^\theta \quad (104)$$

where $\boldsymbol{\varepsilon}^e$ is the elastic strain and θ is the temperature variation. Only the elastic part $\boldsymbol{\varepsilon}^e$ of the strain tensor contributes to the elastic energy density [Kuhn \(2013\)](#):

$$\Psi = \frac{1}{2}(s^2 + \eta)\boldsymbol{\varepsilon}^e : [\mathbb{C} : \boldsymbol{\varepsilon}^e] = \frac{1}{2}(s^2 + \eta)(\boldsymbol{\varepsilon} - \boldsymbol{\varepsilon}^\theta) : [\mathbb{C} : (\boldsymbol{\varepsilon} - \boldsymbol{\varepsilon}^\theta)] \quad (105)$$

The Cauchy stress is then expressed in terms of the total and thermal strains:

$$\boldsymbol{\sigma} = \frac{\partial \Psi}{\partial \boldsymbol{\varepsilon}} = \frac{1}{2}(s^2 + \eta)\mathbb{C} : (\boldsymbol{\varepsilon} - \boldsymbol{\varepsilon}^\theta) \quad (106)$$

The crack evolution equation in [Kuhn and Müller \(2008\)](#) then can be modified as

$$\dot{s} = -M \left\{ s(\boldsymbol{\varepsilon} - \boldsymbol{\varepsilon}^\theta) : [\mathbb{C} : (\boldsymbol{\varepsilon} - \boldsymbol{\varepsilon}^\theta)] - G_c \left(2\epsilon\Delta s + \frac{1-s}{2\epsilon} \right) \right\} \quad (107)$$

In addition to the balance equation and phase field evolution equation, the governing equation for the temperature field is ([Kuhn 2013](#)):

$$-\nabla \cdot \mathbf{q}^\theta = \rho c \dot{\theta} \quad (108)$$

where c is the specific heat capacity and \mathbf{q}^θ is the heat flux. [Kuhn and Müller \(2009\)](#) considered the influence of the phase field on the heat conduction behavior and the modified Fourier's law

can be expressed as follows

$$\mathbf{q}^\theta = - (\beta(s^2 + \eta - 1) + 1) \boldsymbol{\kappa} \nabla \theta \quad (109)$$

where $\beta \in [0, 1]$ is a parameter that defines the influence of the crack field on the thermal conductivity $\boldsymbol{\kappa}$. If $\beta = 0$, the heat conduction is not affected by the phase field. If $\beta = 1$, the thermal conductivity degrades and tends to zero for $s = 0$. Consequently, there is no heat flux across a crack, i.e. cracks are isolating (Kuhn 2013).

The thermally induced phase field patterns can be seen in Bourdin (2007); Corson et al. (2009). Badnava et al. (2018) made a recent contribution. They adopted the similar decomposition technology of Miehe et al. (2010a) to the elastic parts of the strain:

$$\boldsymbol{\varepsilon}_\pm^e = \sum_{I=1}^3 \langle \boldsymbol{\varepsilon}_I^e \rangle \mathbf{n}_I \otimes \mathbf{n}_I \quad (110)$$

The initial elastic energy density is modified as

$$\Psi_0^e = \Psi_0^{e+} + \Psi_0^{e-} \quad (111)$$

with

$$\Psi_0^{e\pm} = \frac{1}{2} \boldsymbol{\varepsilon}_\pm^e : \mathbb{C} : \boldsymbol{\varepsilon}_\pm^e \quad (112)$$

Dittmann et al. (2020) introduced a framework to simulate porous-ductile fracture in isotropic thermo-elasto-plastic solids and considered large deformations. In the model, they combined a modified Gurson-Tvergaard-Needleman GTN-type plasticity model with a phase-field fracture approach. Therefore, the temperature-dependent growth of voids on micro-scale followed by crack initiation and propagation on macro-scale can be well modeled.

5.8 Hydraulic fracture

PfMs seem to be a valuable alternative for modeling hydraulic fractures (HF) because all advantages of the phase field methods are appealing for HF. PfMs for HF have been proposed for instance in Bourdin et al. (2012); Ehlers and Luo (2017); Heister et al. (2015); Lee et al. (2016); Miehe and Mauthe (2016); Miehe et al. (2015b); Mikelić et al. (2015a,b); Santillán et al. (2017); Wheeler et al. (2014); Wick et al. (2016); Yoshioka and Bourdin (2016); Zhou et al. (2019b); Zhuang et al. (2020). Wheeler et al. (2014) rewrote the energy functional by including poroelastic terms and succeeded in extending the phase field model to porous media. However, the variation in the reservoir and fracture domains with time is treated as a moving boundary problem and thereby extra work is needed for implementation. Later, Mikelić et al. (2015a,b)

fully coupled the three fields: elasticity, phase field, and pressure. They modified the energy functional from their previous work, the flow in their entire system is governed by Biot equations. The permeability tensor was also modified to consider a higher permeability along the fracture. The implementation approaches of Mikelić et al. (2015a,b) were then enhanced using adaptive element schemes by (Heister et al. 2015; Lee et al. 2016). Wick et al. (2016); Yoshioka and Bourdin (2016) proposed approaches to couple the phase field model to reservoir simulators. Miehe et al. (Miehe and Mauthe 2016; Miehe et al. 2015b) proposed new minimization and saddle point principles for Darcy-Biot-type flow in fractured poroelastic media coupled with phase field modeling. The evolution of the phase field was driven by the effective stress in the solid skeleton and a stress threshold was set. Moreover, the flow in the fractures was set as Poiseuille-type by modeling Darcy flow with an anisotropic permeability tensor. Recently, Ehlers and Luo (2017) embedded a phase-field approach in the theory of porous media to model dynamic hydraulic fracturing. Santillán et al. (2017) proposed an immersed-fracture formulation for impermeable porous media.

Lee et al. (2018b) presented a framework that couples the fluid-filled fracture propagation and a genetic inverse algorithm for optimizing hydraulic fracturing scenarios in porous media. Lee et al. (2018a) proposed an immiscible two phase flow fracture model, based on a traditional phase-field model for predicting fracture initiation and propagation in porous media. The multifluid model extends the classical flow models and nonzero capillary pressure is considered. Mikelić et al. (2019) studied propagation of hydraulic fractures using the fixed stress splitting method. The mechanical step involving displacement and phase field unknowns is studied under a given pressure. However, these recently developed approaches for extending PFM to HF are quite complicated and computationally expensive.

Another interesting work can be seen in Zhou et al. (2018c). Biot poroelasticity theory is applied on the porous medium with a phase field description of the fracture behavior. An additional pressure-related term is added to the original energy functional presented by Miehe et al. (2010a). However, different from Miehe and Mauthe (2016); Miehe et al. (2015b), only the elastic energy drives the fracture propagation and no stress threshold is imposed in the formulation. In addition, the phase field is used to construct indicator functions to transit fluid property from the intact medium to the fully broken one. Zhou et al. (2018c) implemented the phase field modelling by using the aforementioned Comsol Multiphysics and a staggered scheme. The numerical results are also verified by analytical solutions.

The modified energy functional in Zhou et al. (2018c) reads

$$E(\mathbf{u}, \Gamma) = \int_{\Omega} \Psi_e(\boldsymbol{\varepsilon}) d\Omega - \int_{\Omega} \alpha p \cdot (\nabla \cdot \mathbf{u}) d\Omega + \int_{\Gamma} G_c dS - \int_{\Omega} \mathbf{b} \cdot \mathbf{u} d\Omega - \int_{\partial\Omega_h} \mathbf{f} \cdot \mathbf{u} dS \quad (113)$$

where p is the fluid pressure, α is the Biot coefficient, \mathbf{b} is the body force, and \mathbf{f} is the surface

traction on the Neumann boundaries.

The degradation of the elastic energy is modeled by the following equation:

$$\Psi_e(\boldsymbol{\varepsilon}) = [(1 - k)(1 - \phi)^2 + k] \Psi_0^+(\boldsymbol{\varepsilon}) + \Psi_0^-(\boldsymbol{\varepsilon}) \quad (114)$$

where $0 < k \ll 1$ is a model parameter that prevents the tensile part of the elastic energy density from vanishing and avoids numerical singularity when the phase field ϕ tends to 1. The same decomposition as [Miehe et al. \(2010a\)](#) is used to obtain Ψ_0^+ , Ψ_0^- , $\boldsymbol{\varepsilon}_+$, and $\boldsymbol{\varepsilon}_-$.

With the first variation of the energy functional and the history reference field $H(\boldsymbol{x}, t) = \max_{\tau \in [0, t]} \psi_0^+(\boldsymbol{\varepsilon}(\boldsymbol{x}, \tau))$ being used, the strong form is written as

$$\left\{ \begin{array}{l} \frac{\partial \sigma_{ij}^{por}}{\partial x_i} + b_i = 0 \\ \left[\frac{2l_0(1 - k)H}{G_c} + 1 \right] \phi - l_0^2 \frac{\partial^2 \phi}{\partial x_i^2} = \frac{2l_0(1 - k)H}{G_c} \end{array} \right. \quad (115)$$

with the Cauchy stress tensor $\boldsymbol{\sigma}^{por} = \boldsymbol{\sigma}(\boldsymbol{\varepsilon}) - \alpha p \mathbf{I}$.

Recently, new PFMs are developed for hydraulic fractures. For example, [Shiozawa et al. \(2019\)](#); [Zhou et al. \(2020\)](#) considered the effect of stress boundary in the phase field models and the correct HF type under stress boundary can be well predicted. [Zhou and Zhuang \(2020\)](#) proposed a phase field model for hydraulic fracturing in transversely isotropic porous media.

5.9 length scale insensitive phase-field model

[Wu and Nguyen \(2018\)](#) extended their work in quasi-brittle failure and proposed for the first time a length scale insensitive phase-field model for brittle fracture. Their model involves a phase-field regularized cohesive zone model (CZM) with linear softening law and several optimal characteristic functions. As an extension of the common phase field models, the length scale insensitive model has both failure strength and traction-separation law that are independent of the internal length scale parameter. The best merit of the proposed model is that it gives length scale independent global responses for fracture problems.

5.10 Rock fracture

[Choo and Sun \(2018\)](#) combined a pressure-sensitive plasticity model and a phase field model to model fractures in geological materials. [Zhou et al. \(2019a\)](#) revisited the formulation of [Ambati et al. \(2015b\)](#) and established a new driving force for the phase field evolution to consider compressive-shear fractures in rocks. The phase field model is established in a hybrid framework. To the authors' best knowledge, the model is the first model that can simulate well the

compression-induced fracture in rocks and consider the friction effect. [Fei and Choo \(2020\)](#) developed another phase field model for shear fracture in pressure-sensitive geomaterials with emphasis on the effect of friction on fracture evolution. Governing equations for different contact conditions are established while energy is assumed dissipated during slip. The degradation function and threshold energy are fully considered such that the stress responses are insensitive to the length scale. However, the fracture direction is not automatically determined by the evolution equation of the phase field. Instead, the direction is determined using an extra criterion. [Wang et al. \(2020\)](#) proposed a phase-field model for mixed-mode fracture based on a unified tensile fracture criterion. The proposed method can be also applied to rock fracture. The model involves an additional material parameter. However, the fracture angle is determined by the tensile fracture criterion.

6 Representative numerical examples

In this section, some representative examples are presented to show the capability of the phase field modeling of fracture.

6.1 Single-phasic problem

6.1.1 Quasi-static fracture

1. 2D notched square plate subjected to tension Fracture patterns in a square plate with an initial notch subjected to static tensile loading are presented in Fig. 4 ([Zhou et al. 2018a](#)). This benchmark test has been calculated and analyzed by [Hesch and Weinberg \(2014\)](#); [Liu et al. \(2016\)](#); [Miehe et al. \(2010a,b\)](#). The geometry and loading condition are shown in Fig. 4a. The material parameters are: Young’s modulus $E = 210$ GPa, Poisson’s ratio $\nu = 0.3$, and critical energy release rate $G_c = 2700$ J/m². Figure 4b and c shows a horizontal cracks in the middle of the plate.

The effects of different phase field models on this tension example are also tested. We show the results obtained from [Miehe et al. \(2010b\)](#), [Ambati et al. \(2015b\)](#), [Amor et al. \(2009\)](#) and the isotropic model under length scale $l_0 = 1.5 \times 10^{-2}$ mm and maximum mesh size $h = 7.5 \times 10^{-3}$ mm. The numerical simulations indicate that all the mentioned four PFMs can obtain the same fracture pattern. However, the fracture initiation and propagation differ at the same vertical displacement as shown in Fig. 5. In addition, different PFMs show different load-displacement curves as shown in Fig 6. [Amor et al. \(2009\)](#) predicts a much higher peak load compared with the other methods.

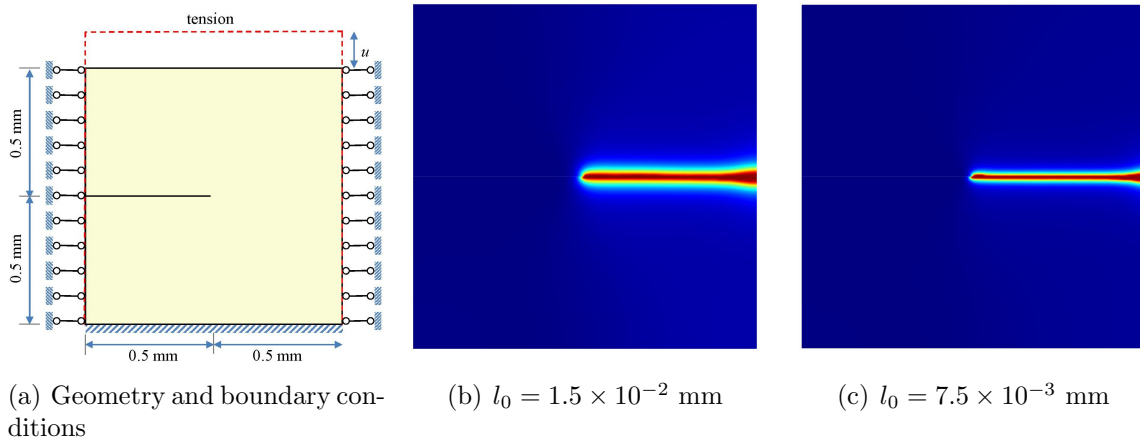


Fig. 4 Fracture patterns of a single-edge-notched square plate subjected to tension (Zhou et al. 2018a)

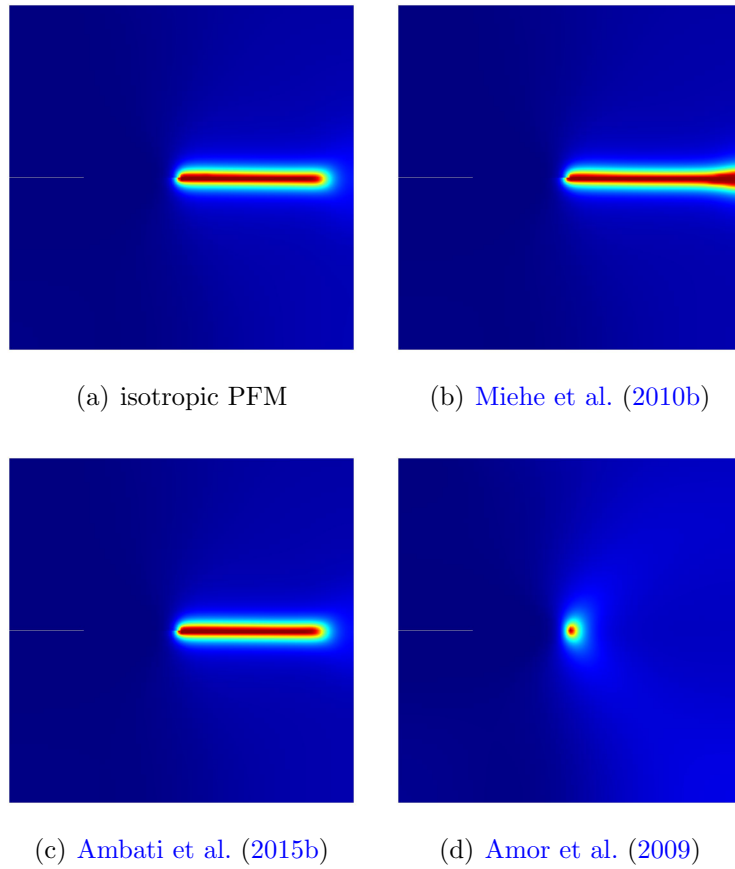


Fig. 5 Fracture patterns of a single-edge-notched square plate subjected to tension when $u = 6.2 \times 10^{-3}$ mm

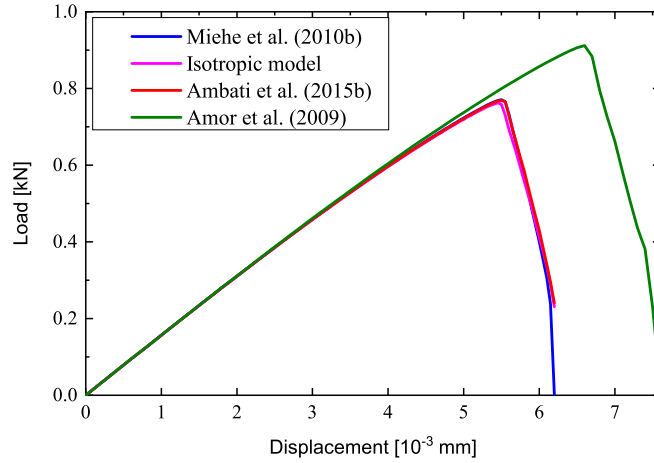


Fig. 6 Load-displacement curve of a single-edge-notched square plate subjected to tension for different PFMs

2. 2D notched square plate subjected to shear Fracture patterns in a square plate with an initial notch subjected to static shear loading are presented in Fig. 7 (Zhou et al. 2018a). This benchmark test is also shown in Hesch and Weinberg (2014); Liu et al. (2016); Miehe et al. (2010a,b). The geometry and loading condition are shown in Fig. 7a. Figure 7b and c shows an inclined crack from the right tip of the pre-existing notch. As expected, the crack has a larger width when $l_0 = 1.5 \times 10^{-2}$ mm.

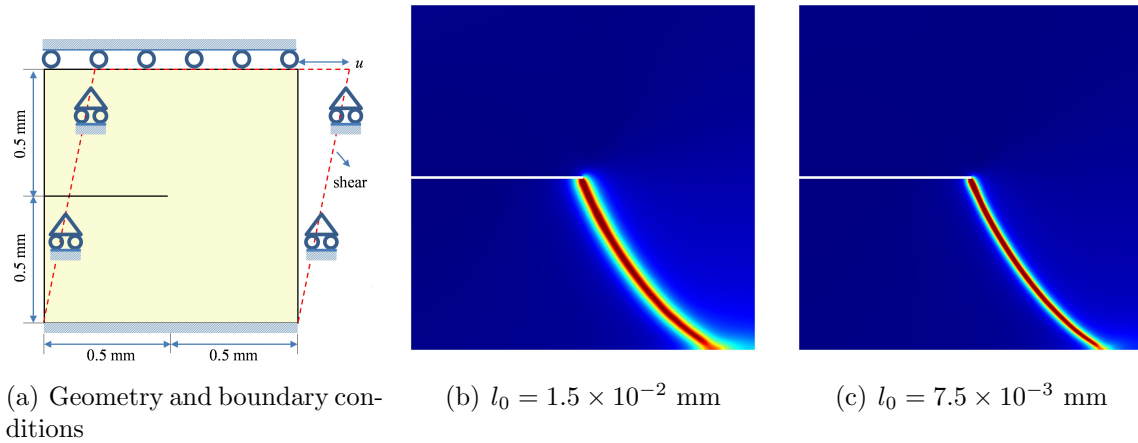


Fig. 7 Fracture patterns of a single-edge-notched square plate subjected to shear (Zhou et al. 2018a)

The performance of the models of Miehe et al. (2010b), Ambati et al. (2015b), Amor et al. (2009) and the isotropic model on the shear example is also tested. Note that the same parameters in the tension example are used. Figure 8 shows the final fracture patterns obtained by

different phase field models. [Miehe et al. \(2010b\)](#) and [Ambati et al. \(2015b\)](#) obtain a similar inclined shear fracture while the isotropic model and [Amor et al. \(2009\)](#) achieve a horizontal pure mode II fracture. The load-displacement curves for shear are shown in Fig. 9. Compared with the isotropic model and [Amor et al. \(2009\)](#), the plate can sustain to a larger shear load when the models of [Miehe et al. \(2010b\)](#) and [Ambati et al. \(2015b\)](#) are applied.

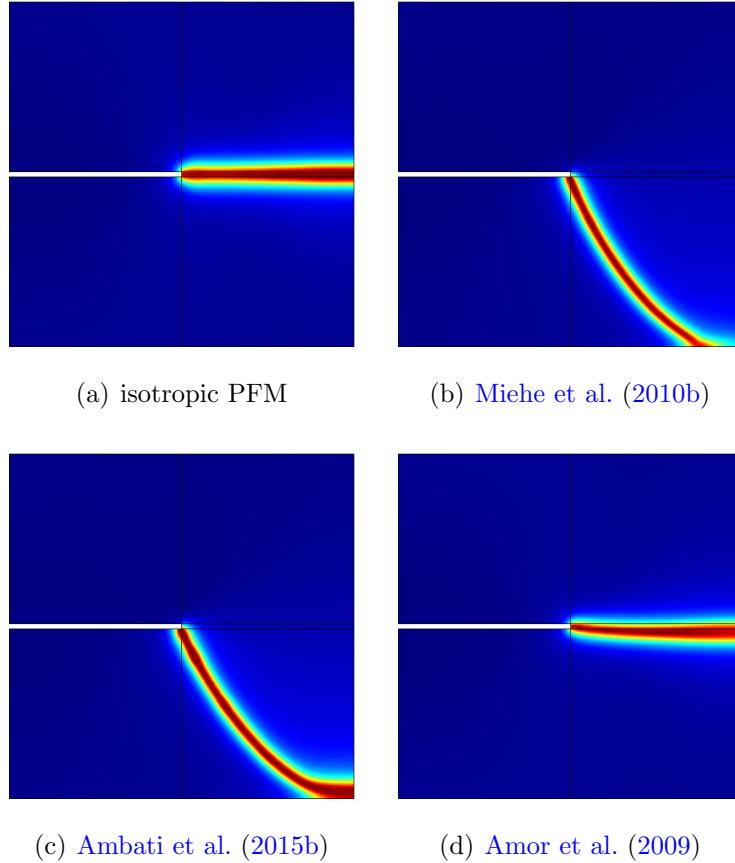


Fig. 8 Fracture patterns of a single-edge-notched square plate subjected to shear: different PFMs

3. 2D notched square plate subjected to tension and shear This example shows fractures in a double-edge-notched plate subjected to both tension and shear loading. Figure 10a shows the geometry and boundary conditions. The length, height and thickness of the plate are 200, 200 and 50 mm, respectively. Two horizontal notches are 25 mm \times 5 mm. More details can be referred to [Zhou et al. \(2018a\)](#). Figure 10b to 10e shows the fracture patterns under different critical energy release rates, i.e. $G_c = 25, 50, 75$ and 100 J/m², respectively.

4. 2D notched semi-circular bend (NSCB) test Fracture patterns in a 2D notched semi-circular bend (NSCB) test are simulated by [Zhou et al. \(2018d\)](#) and the predicted results are

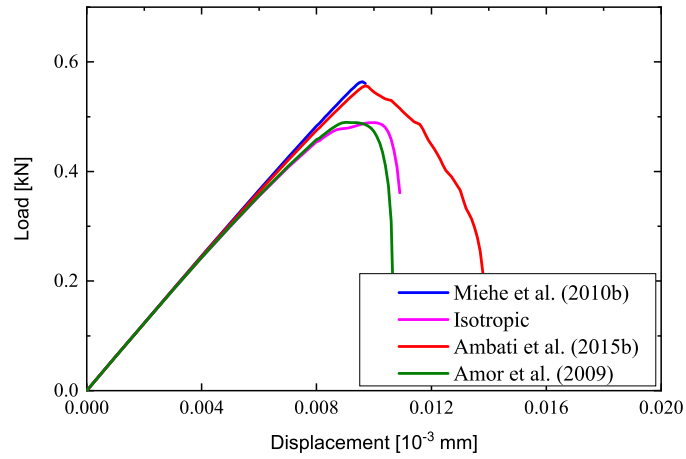


Fig. 9 Load-displacement curve of a single-edge-notched square plate subjected to shear for different PFMs

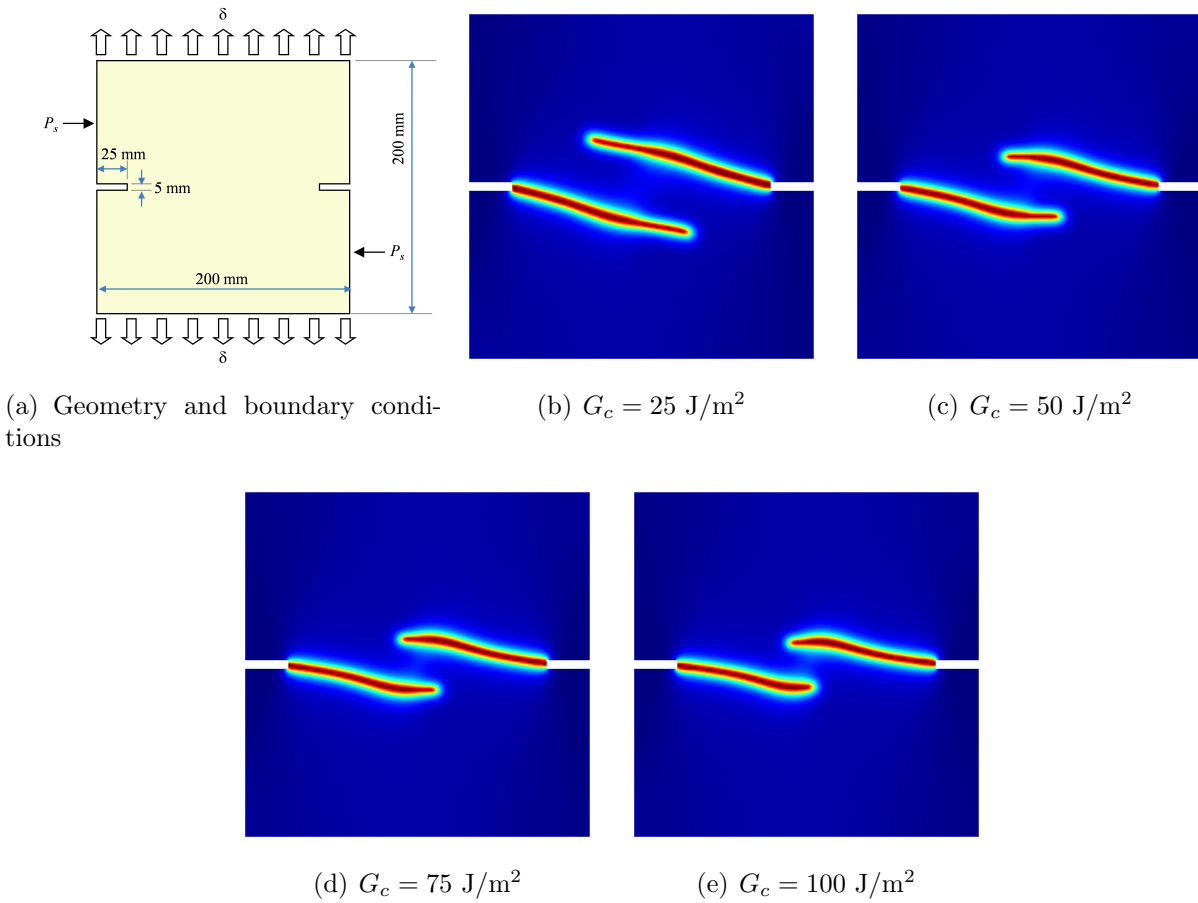


Fig. 10 Fracture patterns of a notched square plate subjected to tension and shear (Zhou et al. 2018a)

presented in Fig. 11. The geometry and loading condition are shown in Fig. 11a. As shown in Fig. 11b, the fracture initiates from the upper tip of the pre-existing notch and propagates along the vertical direction. This observation is in good agreement with those in experimental tests (Gao et al. 2015).

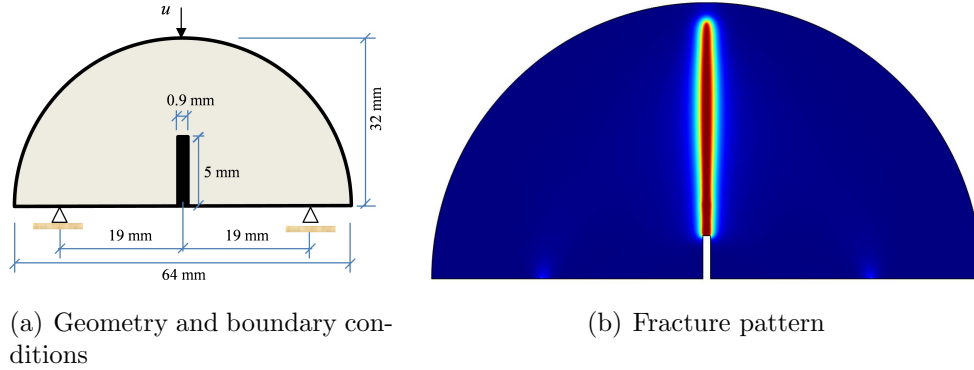


Fig. 11 Fracture patterns of a 2D notched semi-circular bend (NSCB) test (Zhou et al. 2018d)

5. Propagation of multiple echelon flaws This example shows a square plate with nine echelon flaws subjected to tension. The geometry and boundary conditions are shown in Fig. 12a. As observed, these flaws have the same inclination angle of 45° and a varying length and spacing. The final fracture pattern is shown in Fig. 12b. Fractures from the bottom flaws are dominated due to the stress shielding and amplification effects from flaw interaction.

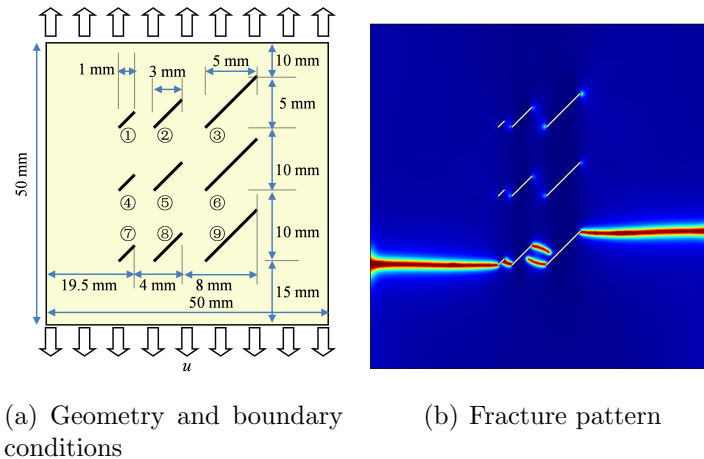


Fig. 12 Fracture patterns of a square plate with nine echelon flaws subjected to tension (Zhou et al. 2018d)

6. Propagation and coalescence of twenty parallel flaws This example shows a square plate with twenty parallel flaws subjected to tension and the fracture patterns are simulated by Zhou et al. (2018d) by using the anisotropic phase field model. With the geometry and boundary conditions being shown in Fig. 13a, symmetric fractures are depicted in Fig. 13b. In addition, fractures only initiate from the upper and bottom flaws and there are no interior fractures.

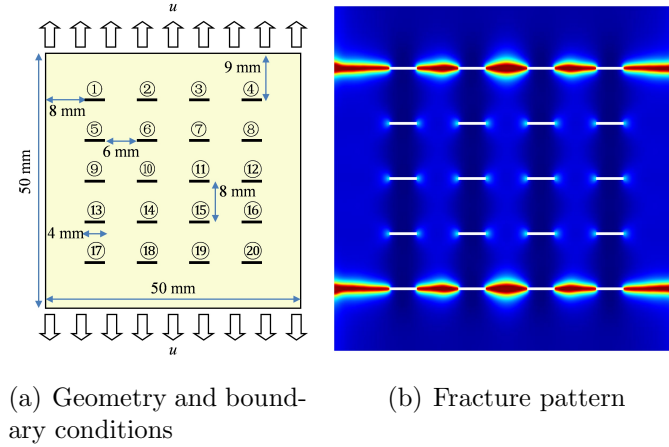


Fig. 13 Fracture patterns of a square plate with twenty parallel flaws subjected to tension (Zhou et al. 2018d)

7. Propagation and coalescence of three parallel flaws in Brazilian discs In a Brazilian splitting test, a plane cylinder specimen is subjected to diametral compression (Zhou 2018). Zhou (2018) used the phase field method to investigate the fracture propagation in Brazilian discs with multiple pre-existing notches. The specimen and flaw dimensions can be found in Zhou (2018). Figure 14 shows the final crack patterns of the Brazilian discs with three vertically arranged notches under different notch spacing. Outer cracks initiate from the notch tips and propagate towards the disc ends. The crack propagation intersects with the vertical direction at a small angle. When the spacing $S = 1$ cm, only one inner crack occurs between two adjoining notches. However, for $S = 3$ cm, the two inner cracks from the inner tips of the notches coalesce.

Figure 15 shows the final crack patterns of the Brazilian discs with three horizontal notches and the influence of different notch spacing. For $S = 2$ cm and $S = 3$ cm, the cracks are similar. The phase field modelling only shows two outer cracks that propagate towards the two ends of the specimen. However, for $S = 1$ cm, additional inner cracks initiate from the notch tips and evolves between two adjoining notches.

8. Compressive-shear fracture Rock is a typical geological material and compressive-shear fractures can be formed in rocks during loading. Zhou et al. (2019a) proposed a phase field model for simulating compressive-shear fracture. Here, we compare the model of Zhou et al.

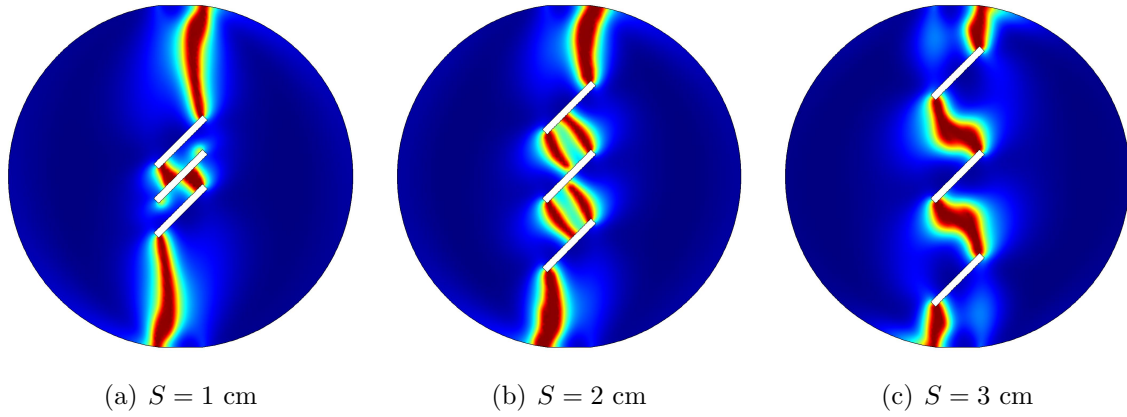


Fig. 14 Fracture patterns of a Brazilian disc with three vertical parallel flaws (Zhou 2018)

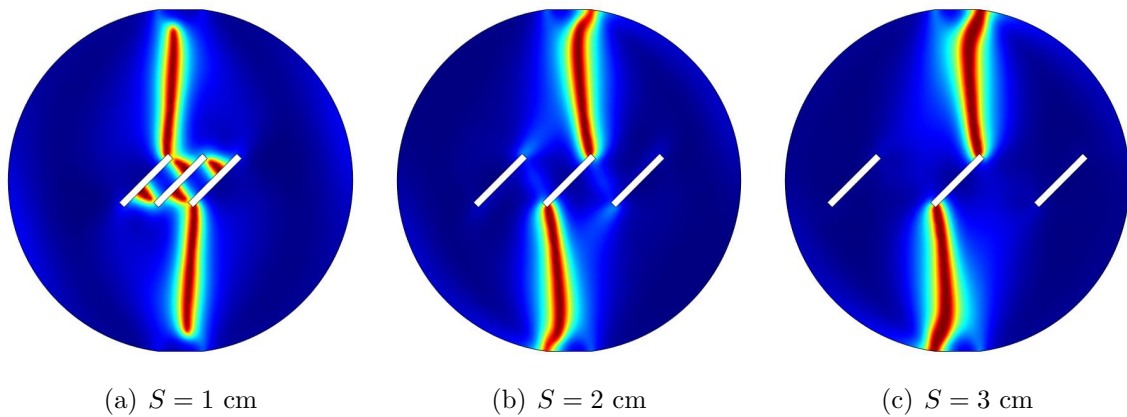


Fig. 15 Fracture patterns of a Brazilian disc with three horizontal parallel flaws (Zhou 2018)

(2019a) and the anisotropic model of Miehe et al. (2010b). The fracture pattern and load-displacement curves are shown in 16 under the same elastic and fracture parameters. In Fig. 16, the anisotropic model of (Miehe et al. 2010b) does not have a drop stage in the load-displacement curve while the model of Zhou et al. (2019a) has an obvious drop stage. Moreover, only wing and anti-wing tensile cracks are simulated in the model of (Miehe et al. 2010b) while the model of Zhou et al. (2019a) predicts well the compressive-shear fracture in rocks.

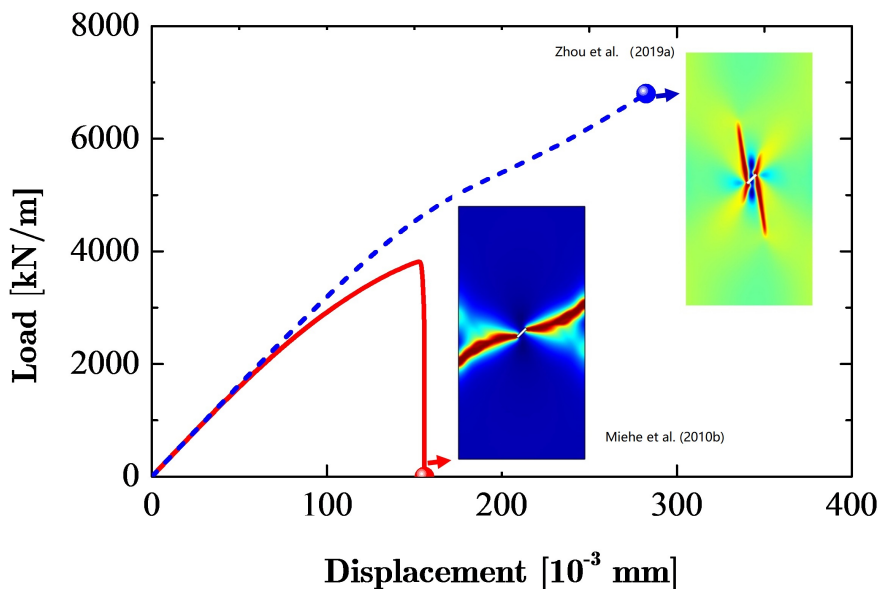


Fig. 16 Comparison of fracture pattern and load-displacement curve

6.1.2 Dynamic fracture

1. 2D dynamic shear loading of Kalthoff experiment The phase field method has been used in Kalthoff experiment (Borden et al. 2012; Liu et al. 2016; Zhou et al. 2018a) and its geometry and boundary condition are shown in Fig. 17a. The influence of the critical energy release rate G_c on the phase field is shown in Fig. 17b to 17e according to the results of Zhou et al. (2018a). As observed, a smaller G_c produces more complex crack patterns. Crack branching occurs for $G_c = 5 \times 10^3$ and 1×10^4 J/m². Whereas, for a larger G_c , the phase field simulation only show a single crack. The distance of the crack tip from the upper boundary of the plate increases as G_c increases. Figure 18 shows the crack-tip velocity under different G_c . As observed, the maximum crack-tip velocity decreases with an increasing G_c but the time of crack initiation increases (Zhou et al. 2018a).

2. 2D dynamic crack branching under tension This example is a pre-notched rectangular plate subjected to uniaxial traction and has been investigated by Borden et al. (2012); Liu et al.

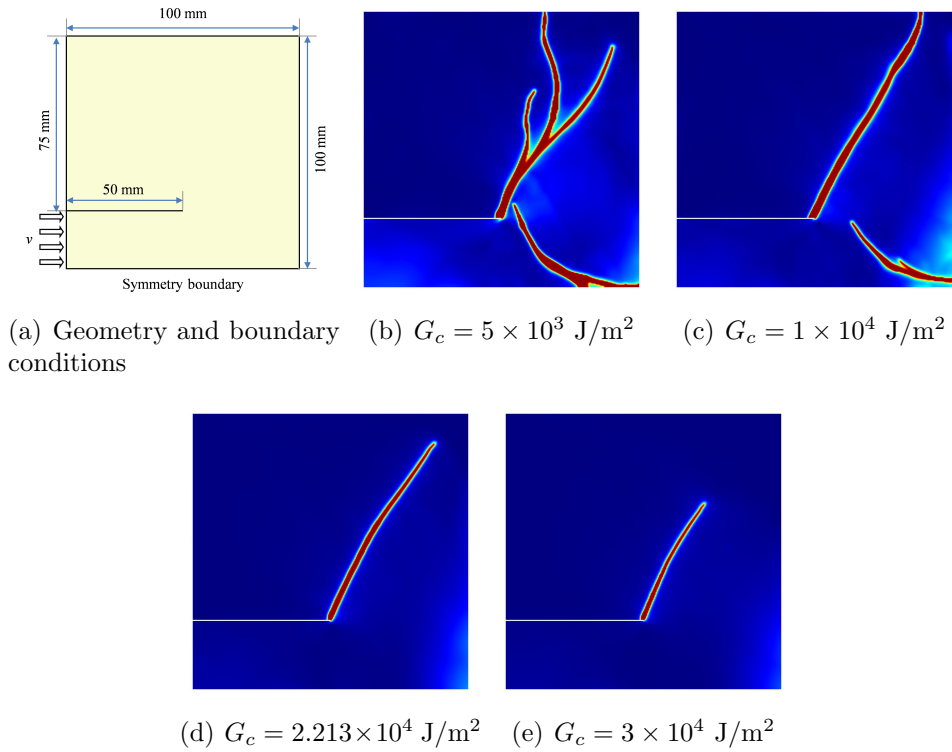


Fig. 17 Phase field of dynamic shear loading tests at $90 \mu\text{s}$ for different G_c (Zhou et al. 2018a)

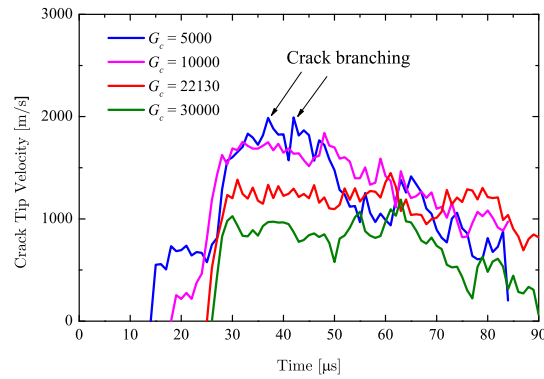


Fig. 18 Crack-tip velocity of the dynamic shear loading example for different G_c (Zhou et al. 2018a)

(2016); Zhou et al. (2018a). Geometry and boundary condition of the pre-notched plate are given in Fig. 19. The influences of the critical energy release rate G_c on the crack pattern and the crack-tip velocity are shown in Figs. 20 and 21. As observed, multiple crack branching occurs for different G_c . In addition, the crack propagates at a larger angle with the horizontal after the first crack branching under a larger G_c . The maximum crack-tip velocity in Fig. 21 decreases with the increase in G_c .

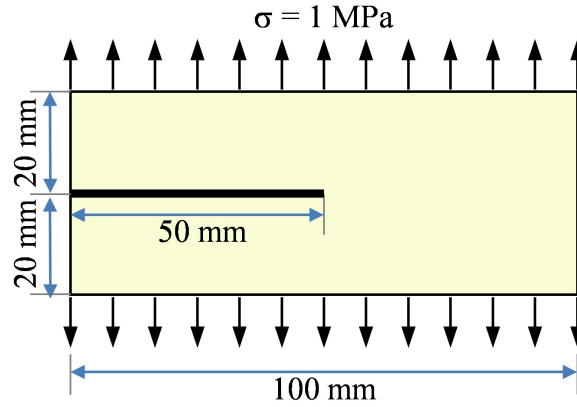


Fig. 19 Geometry and boundary conditions for the case of dynamic crack branching (Zhou et al. 2018a)

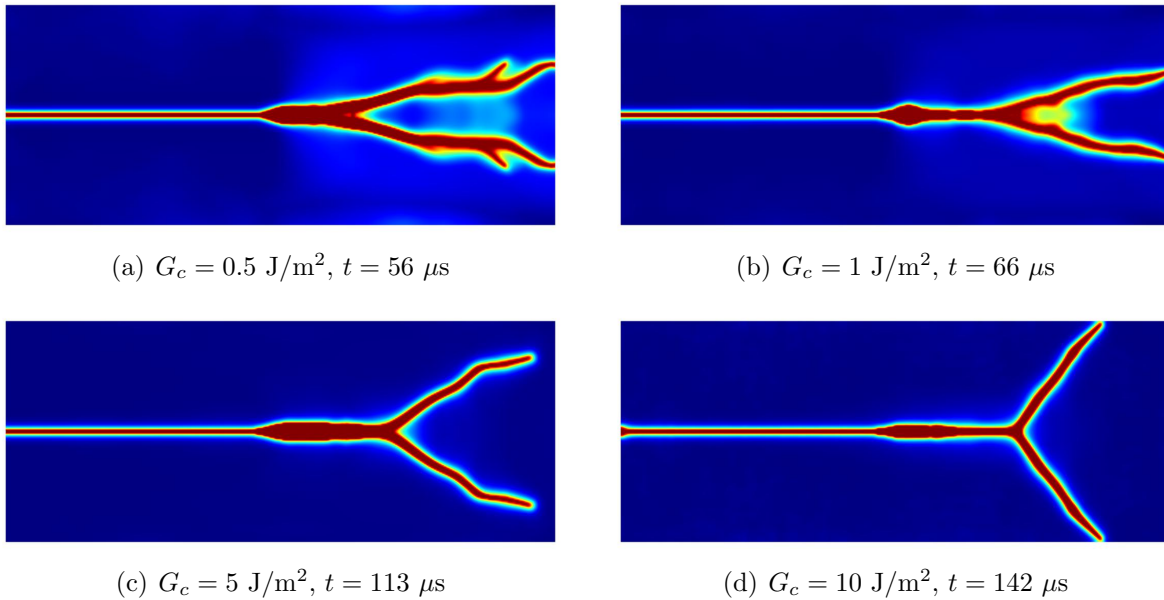


Fig. 20 Crack patterns of the 2D crack branching example for different G_c (Zhou et al. 2018a)

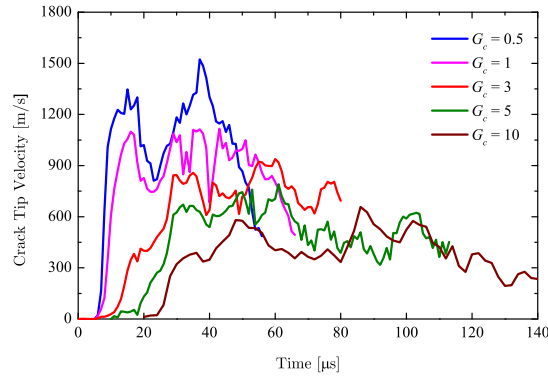


Fig. 21 Crack-tip velocity of the 2D crack branching example for different G_c (Zhou et al. 2018a)

6.2 Hydraulic fracture

6.2.1 Propagation of a single crack by internal fluid injection

This example shows propagation of one single pre-existing crack when fluid is injected. The crack is placed horizontally at the center of a square specimen of $4 \text{ m} \times 4 \text{ m}$. The initial length of the crack is 0.4 m and the displacements on the outer boundaries of the square are fixed with the fluid pressure $p = 0$. Q4 elements are used to discretize all the fields with element size $h = 2 \times 10^{-2} \text{ m}$. Here, we used the same method and parameters in Zhou et al. (2018c) to simulate the crack pattern and pressure field.

The fracture pattern at $t = 8.8 \text{ s}$ is shown in Fig. 22a. As expected, the single pre-existing crack propagates along the horizontal direction, in good agreement with the results of Mikelić et al. (2015a) and Mikelić et al. (2015). The pressure distribution at $t = 8.8 \text{ s}$ is presented in Fig. 22b. The pressure field is similar to the phase field in Fig. 22a. However, the region where the pressure concentrates is larger than the cracked region because of the radial penetration of the fluid is used in Zhou et al. (2018c).

6.2.2 Two parallel propagating cracks subjected to internal fluid injection

This example shows propagation of two parallel pre-existing cracks when fluid is injected. Geometry and boundary conditions of this example are shown in Fig. 23a. The two pre-existing cracks are 1 m in length and have a spacing of 0.6 m . Q4 elements are used to discretize all the fields with the element size $h = 2 \times 10^{-2} \text{ m}$. The evolution of the phase field is presented in Fig. 23b. The spacing of the propagating cracks increases with increasing time. The pressure distribution is shown in Fig. 23c. The pressure is similar to the phase field but has a larger transition band.

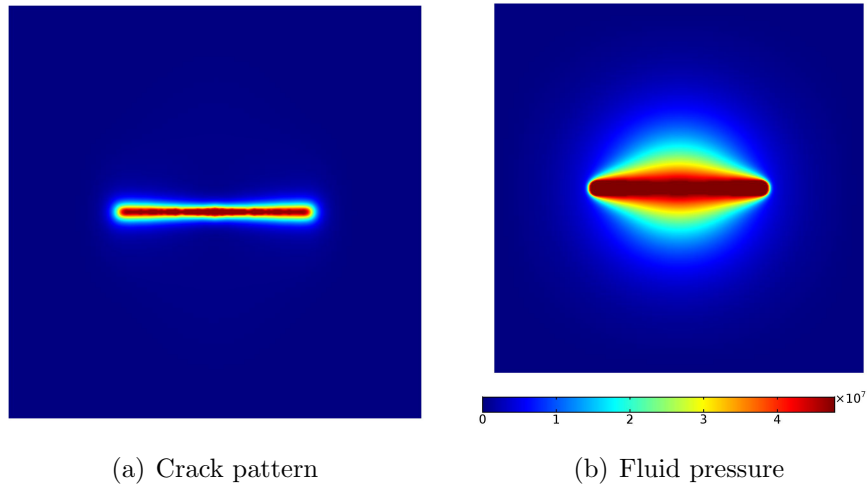


Fig. 22 Crack pattern and fluid pressure for the example of one single pre-existing crack subjected to internal fluid injection at $t = 8.8$ s

6.2.3 Three parallel propagating cracks in 2D

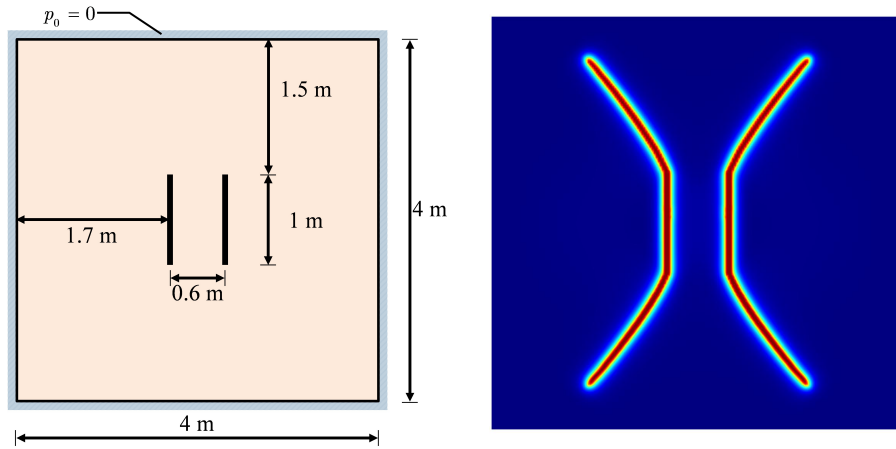
Crack propagation of three propagating cracks in 2D is simulated by the phase field model. The geometry and boundary conditions are given in Fig. 24a. The three cracks have the same length of 1 m and a spacing of 1 m. Uniformly spaced Q4 elements with size $h = 2 \times 10^{-2}$ m are employed. The crack pattern is shown in Fig. 24b. No propagation is found for the middle crack and only the left and right cracks propagate. The pressure distribution is shown in Fig. 24c. The pressure in the middle crack is much larger than that in the left and right cracks because the middle crack barely propagates.

6.2.4 Propagation of two parallel penny-shaped cracks in 3D

This example verifies the capability of the phase field modeling for hydraulic fractures in 3D. Two parallel penny-shaped cracks are set in the domain of $(-2 \text{ m}, 2 \text{ m})^3$. The initial crack radius is 0.5 m. More details can be referred to Zhou et al. (2018c). Crack propagation patterns of the two parallel penny-shape cracks in 3D are shown in Fig. 25. The radii of the two cracks exceed 0.5 m when $t = 13.2$ s and bowl-shaped cracks are observed when $t = 13.3$ s.

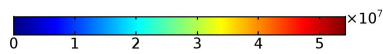
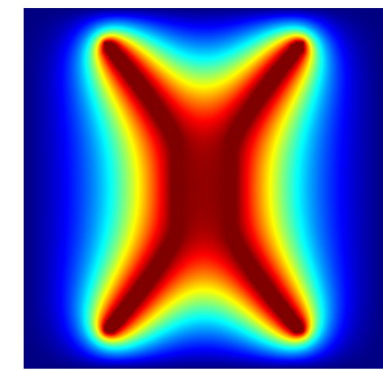
6.3 Fractures in plates and shells

To illustrate the capability of phase field modeling on capturing cracking in thin structures, three representative numerical examples are given with a focus on qualitatively crack paths formed from these examples in this subsection. The employed approach is based on Kiendl et al. (2016), where Kirchhoff-Love thin shell and brittle fracture are considered in linear regime. To



(a) Geometry and boundary condition

(b) Crack pattern



(c) Pressure field

Fig. 23 The example of two parallel pre-existing cracks

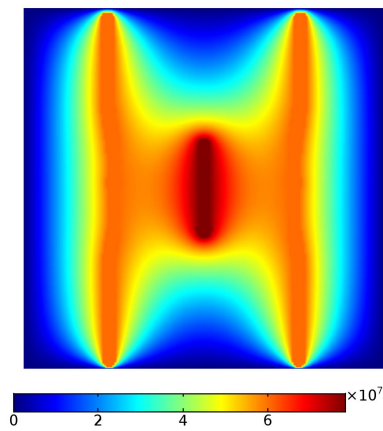
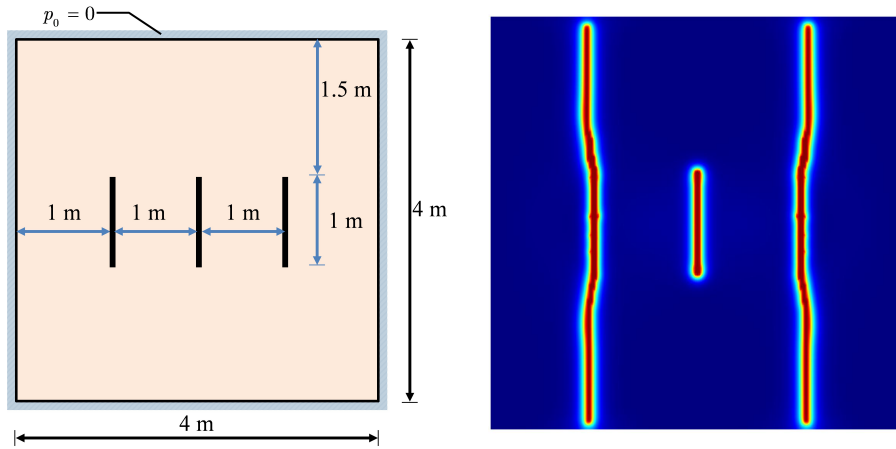


Fig. 24 The example of three parallel pre-existing cracks in 2D

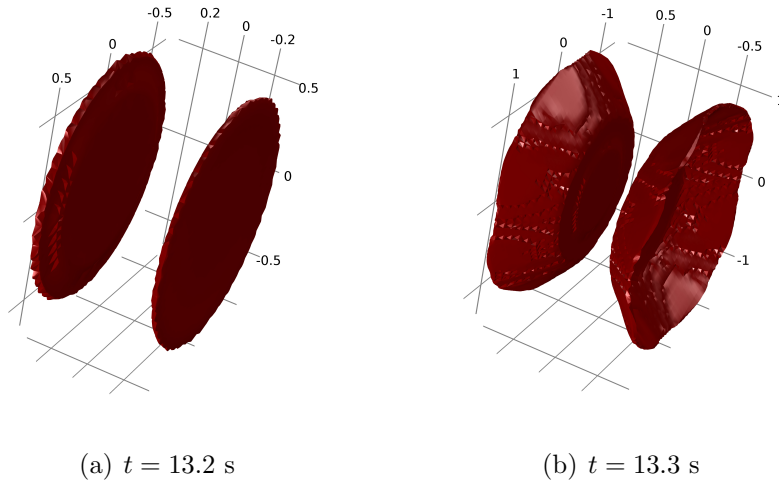


Fig. 25 Crack patterns for the example of two parallel penny-shaped cracks in 3D

accommodate C0-continuity requirement from the shell theory, quadratic NURBS basis functions are used to approximate solution fields.

6.3.1 Single edge notched tension test

First, a square plate consisting of a horizontal notch is considered. The top edge of the specimen is applied vertical displacement. The geometric properties of the plate are depicted in Fig. 26. The material parameters are chosen such that $E = 1$ GPa, $\rho = 0.3$, $G_c = 2$ N/mm and $l_0 = 0.02$ mm. 23,000 elements are used to discretize the analysis domain and refine a priori in expected crack zones. Displacement control method is applied to conduct the simulation with displacement increment $\Delta u = 10^{-6}$ mm for the first 200 loading steps and $\Delta u = 0.5 \times 10^{-6}$ mm for the remaining steps until the specimen are broken completely. Fig. 27 shows the crack patterns at different loading stages. The resulting crack paths are coincident with those obtained from previous works of Ambati and De Lorenzis (2016) and Kiendl et al. (2016). The load-deflection curves for solid and Kirchhoff-Love shell elements in Fig. 28 are comparable to each other and in good agreement with those from Ambati and De Lorenzis (2016).

6.3.2 Simply supported Plate

Next, a square plate without initial cracks subjected to uniform pressure is simply supported on its four edges. The geometry and boundary conditions of the problem are depicted in Fig. 29 and material parameters are chosen as $E = 190$ GPa, $\rho = 0.29$, $G_c = 0.295$ N/mm and $l_0 = 0.02$ mm. The model is discretized with 28,000 elements and $h/l_0 = 1.7$. With such applied load, arc-length control is utilized as a solution strategy to track mechanical response of the structure when crack starts to propagate. The resulting crack patterns are depicted at various stages of

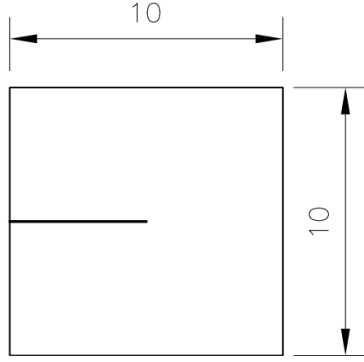


Fig. 26 Tension test. Geometry

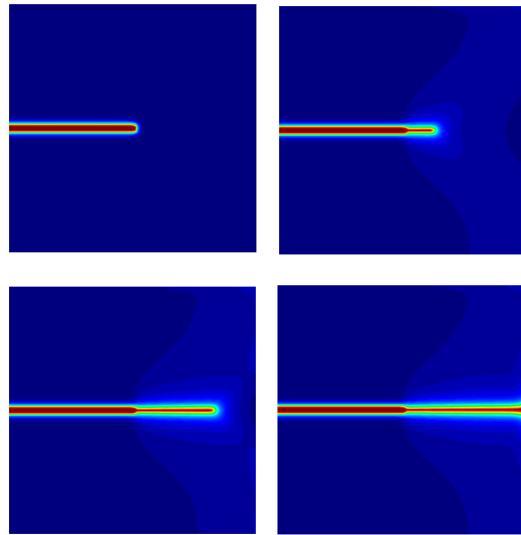


Fig. 27 Tension test. Crack patterns at various loading stages

deformation as in Fig. 30. As can be seen, crack initiation arises at the center and then crack branching occurs, leading to the evolution of cracks towards the corners, which is coincident with observations from previous investigations (Ambati and De Lorenzis 2016; Kiendl et al. 2016). Figure 31 shows the corresponding load-deflection curve, which is in agreement with one obtained by Ambati and De Lorenzis (2016).

6.3.3 Notched cylinder with internal pressure

Finally, a curved shell structure is considered. It consists of two notches in the axial direction, which are located on opposite sides and the shell is subjected to internal pressure. Geometry and boundary condition setups are given in Fig. 32. The material parameters are chosen as $E = 70$ GPa , $\rho = 0.3$, $G_c = 1.5$ N/mm and $l_0 = 0.05$ mm. A mesh with 32,000 elements, which

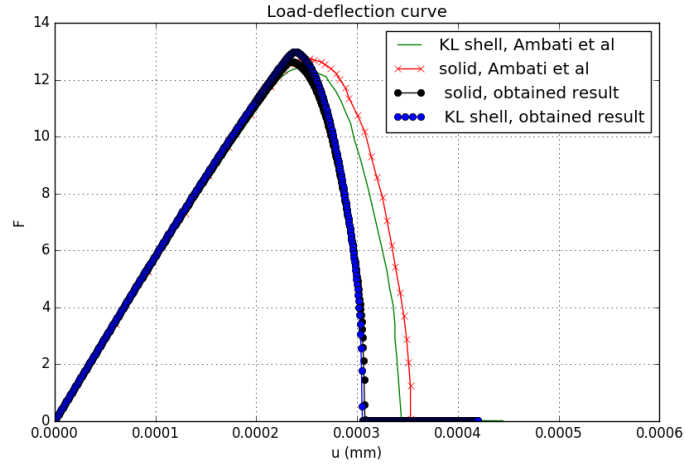


Fig. 28 Tension test. Load-deflection curve

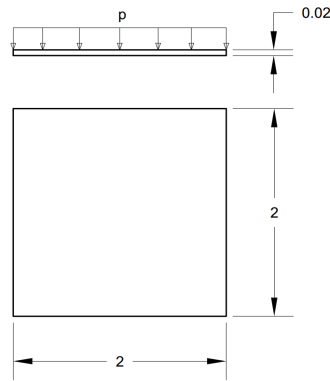


Fig. 29 Square plate. Geometry and boundary condition setups

is refined a priori in the regions where cracks are expected to propagate, is used to discretize the shell structure. Arc-length control is adopted for the simulation. Fig. 33 shows crack phase field at different stages of deformation. As expected, a straight crack propagating axially is observed, which is coincident with those obtained from previous investigations (Ambati and De Lorenzis 2016; Kiendl et al. 2016).

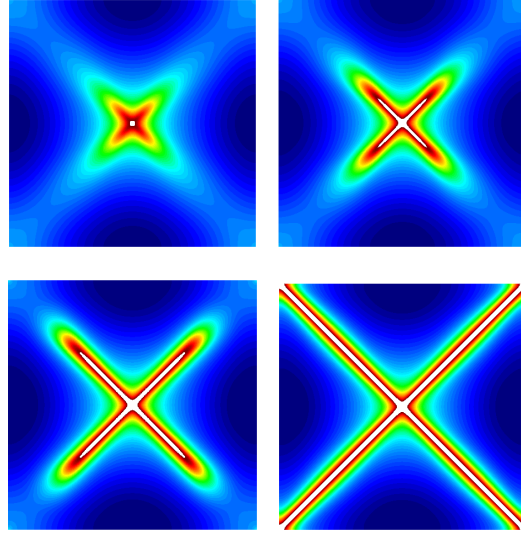


Fig. 30 Simply supported plate. Crack patterns at various loading stages

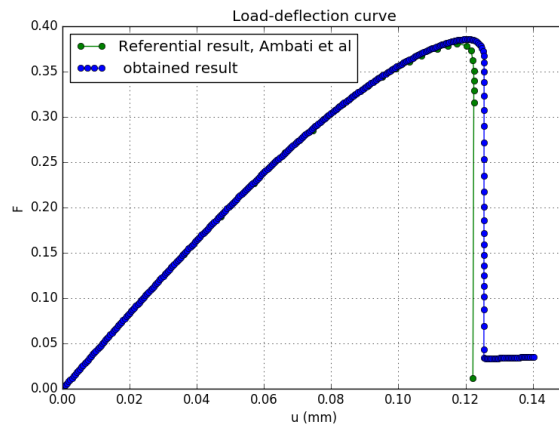


Fig. 31 Square plate. Load-deflection curve

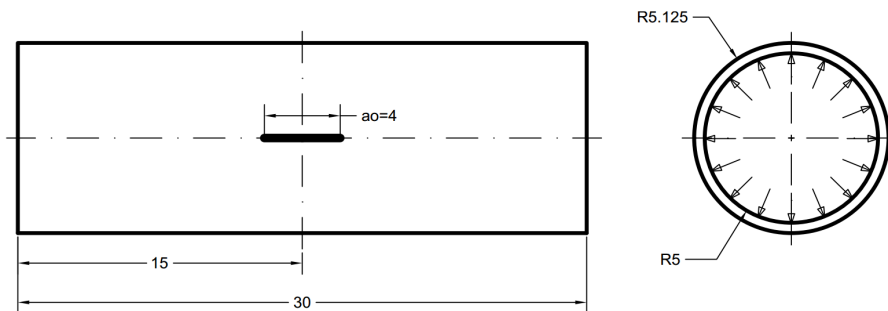


Fig. 32 Notched cylinder with internal pressure. Geometry and boundary condition setups

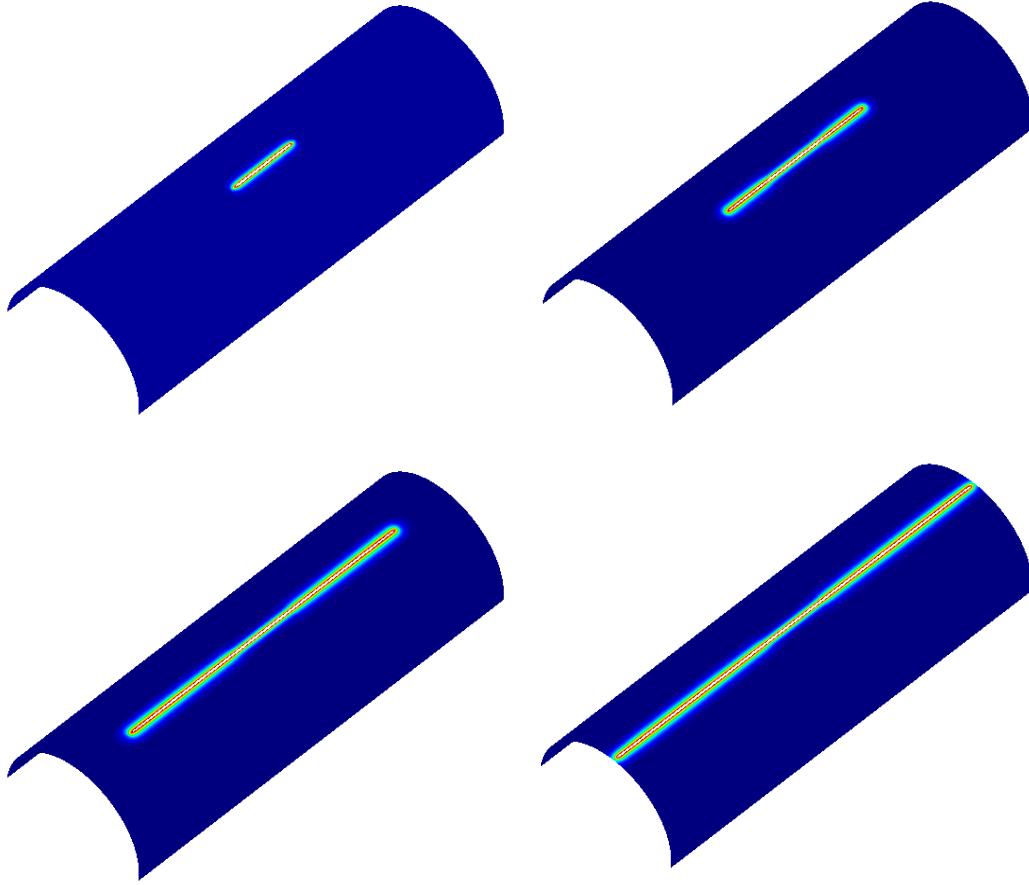


Fig. 33 Notched plate with hole. Crack patterns at different loading stages

7 Conclusions

This work presents an overall picture and some recent progress of the phase field method in modeling fracture initiation and propagation. This work sums up the significant stages during the development of the phase field models of fracture in both physics and mechanics communities. The theory and the use of the phase field models are also shown to demonstrate their advantages of handling complex fracture problems. The phase field models use an additional scalar field (phase field) to represent the discrete cracks rather than introduce directly physical discontinuity. The fracture shape and propagation are only determined from the evolution equations of the phase-field. Compared with other fracture methods, the phase field model does not require additional work to track the fracture surfaces algorithmically and thereby less computational effort is needed for numerical implementation of fracture. Crack branching and merging in materials with arbitrary 2D and 3D geometries can be easily simulated by the phase field models.

Although the phase field model can be coupled with different discretization methods such

as isogeometric analysis and mesh-free methods, most phase field models use the finite element discretization. This work also presents details about computer implementation of the phase field models coupled with finite element methods. Because of the great benefits from the phase field modeling, the phase field models for brittle fractures are extended for solving more complicated problems such as ductile fractures and multi-field problems. In addition, some representative 2D and 3D examples for quasi-static and dynamic fractures are presented to show practicability and capability of the phase field modeling. For future work, the phase field models can be applied in fracture modeling in caverns used for compressed air energy storage (CAES) (Zhou et al. 2015b, 2017a), which shows strong effect of cyclic stress and temperature (Xia et al. 2015; Zhou et al. 2015a, 2018b, 2017b).

Acknowledgement

The authors gratefully acknowledge financial support provided by the Natural Science Foundation of China (51474157), and RISE-project BESTOFRAF (734370).

References

- Aldakheel, F., Hudobivnik, B., Hussein, A., and Wriggers, P. (2018). Phase-field modeling of brittle fracture using an efficient virtual element scheme. *Computer Methods in Applied Mechanics and Engineering*, 341:443–466.
- Alessi, R., Marigo, J.-J., Maurini, C., and Vidoli, S. (2018). Coupling damage and plasticity for a phase-field regularisation of brittle, cohesive and ductile fracture: one-dimensional examples. *International Journal of Mechanical Sciences*, 149:559–576.
- Alessi, R., Marigo, J.-J., and Vidoli, S. (2015). Gradient damage models coupled with plasticity: variational formulation and main properties. *Mechanics of Materials*, 80:351–367.
- Ambati, M. and De Lorenzis, L. (2016). Phase-field modeling of brittle and ductile fracture in shells with isogeometric nurbs-based solid-shell elements. *Computer Methods in Applied Mechanics and Engineering*, 312:351–373.
- Ambati, M., Gerasimov, T., and De Lorenzis, L. (2015a). Phase-field modeling of ductile fracture. *Computational Mechanics*, 55(5):1017–1040.
- Ambati, M., Gerasimov, T., and De Lorenzis, L. (2015b). A review on phase-field models of brittle fracture and a new fast hybrid formulation. *Computational Mechanics*, 55(2):383–405.

- Amiri, F., Millán, D., Arroyo, M., Silani, M., and Rabczuk, T. (2016). Fourth order phase-field model for local max-ent approximants applied to crack propagation. *Computer Methods in Applied Mechanics and Engineering*, 312:254–275.
- Amiri, F., Millán, D., Shen, Y., Rabczuk, T., and Arroyo, M. (2014). Phase-field modeling of fracture in linear thin shells. *Theoretical and Applied Fracture Mechanics*, 69:102–109.
- Amor, H., Marigo, J.-J., and Maurini, C. (2009). Regularized formulation of the variational brittle fracture with unilateral contact: Numerical experiments. *Journal of the Mechanics and Physics of Solids*, 57(8):1209–1229.
- Aranson, I., Kalatsky, V., and Vinokur, V. (2000). Continuum field description of crack propagation. *Physical review letters*, 85(1):118.
- Areias, P., Msekh, M., and Rabczuk, T. (2016a). Damage and fracture algorithm using the screened poisson equation and local remeshing. *Engineering Fracture Mechanics*, 158:116–143.
- Areias, P., Rabczuk, T., and de Sá, J. C. (2016b). A novel two-stage discrete crack method based on the screened poisson equation and local mesh refinement. *Computational Mechanics*, 58(6):1003–1018.
- Areias, P., Rabczuk, T., and Msekh, M. (2016c). Phase-field analysis of finite-strain plates and shells including element subdivision. *Computer Methods in Applied Mechanics and Engineering*, 312:322–350.
- Badnava, H., Msekh, M. A., Etemadi, E., and Rabczuk, T. (2018). An h-adaptive thermo-mechanical phase field model for fracture. *Finite Elements in Analysis and Design*, 138:31–47.
- Bhowmick, S. and Liu, G. R. (2018). A phase-field modeling for brittle fracture and crack propagation based on the cell-based smoothed finite element method. *Engineering Fracture Mechanics*, 204:369–387.
- Bischoff, M., Ramm, E., and Irslinger, J. (2018). Models and finite elements for thin-walled structures. *Encyclopedia of Computational Mechanics Second Edition*, pages 1–86.
- Borden, M. J., Hughes, T. J., Landis, C. M., Anvari, A., and Lee, I. J. (2016). A phase-field formulation for fracture in ductile materials: Finite deformation balance law derivation, plastic degradation, and stress triaxiality effects. *Computer Methods in Applied Mechanics and Engineering*, 312:130–166.

- Borden, M. J., Hughes, T. J., Landis, C. M., and Verhoosel, C. V. (2014). A higher-order phase-field model for brittle fracture: Formulation and analysis within the isogeometric analysis framework. *Computer Methods in Applied Mechanics and Engineering*, 273:100–118.
- Borden, M. J., Verhoosel, C. V., Scott, M. A., Hughes, T. J., and Landis, C. M. (2012). A phase-field description of dynamic brittle fracture. *Computer Methods in Applied Mechanics and Engineering*, 217:77–95.
- Bourdin, B. (2007). The variational formulation of brittle fracture: numerical implementation and extensions. In *IUTAM Symposium on discretization methods for evolving discontinuities*, pages 381–393. Springer.
- Bourdin, B., Chukwudozie, C. P., Yoshioka, K., et al. (2012). A variational approach to the numerical simulation of hydraulic fracturing. In *SPE Annual Technical Conference and Exhibition*. Society of Petroleum Engineers.
- Bourdin, B., Francfort, G. A., and Marigo, J.-J. (2000). Numerical experiments in revisited brittle fracture. *Journal of the Mechanics and Physics of Solids*, 48(4):797–826.
- Braides, A. (2006). A handbook of ϵ -convergence. In *Handbook of Differential Equations: stationary partial differential equations*, volume 3, pages 101–213. Elsevier.
- Bryant, E. C. and Sun, W. (2018). A mixed-mode phase field fracture model in anisotropic rocks with consistent kinematics. *Computer Methods in Applied Mechanics and Engineering*, 342:561–584.
- Chau-Dinh, T., Zi, G., Lee, P.-S., Rabczuk, T., and Song, J.-H. (2012). Phantom-node method for shell models with arbitrary cracks. *Computers & Structures*, 92:242–256.
- Chen, Y., Vasiukov, D., Gélébart, L., and Park, C. H. (2019). A fft solver for variational phase-field modeling of brittle fracture. *Computer Methods in Applied Mechanics and Engineering*, 349:167–190.
- Choo, J. and Sun, W. (2018). Coupled phase-field and plasticity modeling of geological materials: From brittle fracture to ductile flow. *Computer Methods in Applied Mechanics and Engineering*, 330:1–32.
- Corson, F., Adda-Bedia, M., Henry, H., and Katzav, E. (2009). Thermal fracture as a framework for quasi-static crack propagation. *International journal of fracture*, 158(1):1–14.
- de Borst, R. and Verhoosel, C. V. (2016). Gradient damage vs phase-field approaches for fracture: Similarities and differences. *Computer Methods in Applied Mechanics and Engineering*, 312:78–94.

- Dittmann, M., Aldakheel, F., Schulte, J., Schmidt, F., Krüger, M., Wriggers, P., and Hesch, C. (2020). Phase-field modeling of porous-ductile fracture in non-linear thermo-elasto-plastic solids. *Computer Methods in Applied Mechanics and Engineering*, 361:112730.
- Dittmann, M., Aldakheel, F., Schulte, J., Wriggers, P., and Hesch, C. (2018). Variational phase-field formulation of non-linear ductile fracture. *Computer Methods in Applied Mechanics and Engineering*, 342:71–94.
- Duda, F. P., Ciarbonetti, A., Sánchez, P. J., and Huespe, A. E. (2015). A phase-field/gradient damage model for brittle fracture in elastic–plastic solids. *International Journal of Plasticity*, 65:269–296.
- Ehlers, W. and Luo, C. (2017). A phase-field approach embedded in the theory of porous media for the description of dynamic hydraulic fracturing. *Computer Methods in Applied Mechanics and Engineering*, 315:348–368.
- Fang, J., Wu, C., Rabczuk, T., Wu, C., Ma, C., Sun, G., and Li, Q. (2019). Phase field fracture in elasto-plastic solids: Abaqus implementation and case studies. *Theoretical and Applied Fracture Mechanics*, 103:102252.
- Fei, F. and Choo, J. (2020). A phase-field model of frictional shear fracture in geologic materials. *Computer Methods in Applied Mechanics and Engineering*, 369:113265.
- Francfort, G. A. and Marigo, J.-J. (1998). Revisiting brittle fracture as an energy minimization problem. *Journal of the Mechanics and Physics of Solids*, 46(8):1319–1342.
- Fries, T.-P. and Belytschko, T. (2010). The extended/generalized finite element method: an overview of the method and its applications. *International Journal for Numerical Methods in Engineering*, 84(3):253–304.
- Gao, G., Huang, S., Xia, K., and Li, Z. (2015). Application of digital image correlation (DIC) in dynamic notched semi-circular bend (NSCB) tests. *Experimental Mechanics*, 55(1):95–104.
- Geelen, R. J., Liu, Y., Hu, T., Tupek, M. R., and Dolbow, J. E. (2019). A phase-field formulation for dynamic cohesive fracture. *Computer Methods in Applied Mechanics and Engineering*, 348:680–711.
- Gerasimov, T., Noii, N., Allix, O., and De Lorenzis, L. (2018). A non-intrusive global/local approach applied to phase-field modeling of brittle fracture. *Advanced modeling and simulation in engineering sciences*, 5(1):14.

- Goswami, S., Anitescu, C., Chakraborty, S., and Rabczuk, T. (2020a). Transfer learning enhanced physics informed neural network for phase-field modeling of fracture. *Theoretical and Applied Fracture Mechanics*, 106:102447.
- Goswami, S., Anitescu, C., and Rabczuk, T. (2019). Adaptive phase field analysis with dual hierarchical meshes for brittle fracture. *Engineering Fracture Mechanics*, 218:106608.
- Goswami, S., Anitescu, C., and Rabczuk, T. (2020b). Adaptive fourth-order phase field analysis for brittle fracture. *Computer Methods in Applied Mechanics and Engineering*, 361:112808.
- Hakim, V. and Karma, A. (2009). Laws of crack motion and phase-field models of fracture. *Journal of the Mechanics and Physics of Solids*, 57(2):342–368.
- Heister, T., Wheeler, M. F., and Wick, T. (2015). A primal-dual active set method and predictor-corrector mesh adaptivity for computing fracture propagation using a phase-field approach. *Computer Methods in Applied Mechanics and Engineering*, 290:466–495.
- Henry, H. and Levine, H. (2004). Dynamic instabilities of fracture under biaxial strain using a phase field model. *Physical review letters*, 93(10):105504.
- Hesch, C. and Weinberg, K. (2014). Thermodynamically consistent algorithms for a finite-deformation phase-field approach to fracture. *International Journal for Numerical Methods in Engineering*, 99(12):906–924.
- Hofacker, M. and Miehe, C. (2012). Continuum phase field modeling of dynamic fracture: variational principles and staggered fe implementation. *International Journal of Fracture*, pages 1–17.
- Hofacker, M. and Miehe, C. (2013). A phase field model of dynamic fracture: Robust field updates for the analysis of complex crack patterns. *International Journal for Numerical Methods in Engineering*, 93(3):276–301.
- Hossain, M., Hsueh, C.-J., Bourdin, B., and Bhattacharya, K. (2014). Effective toughness of heterogeneous media. *Journal of the Mechanics and Physics of Solids*, 71:15 – 32.
- Ingraffea, A. and Saouma, V. (1985). Numerical modelling of discrete crack propagation in reinforced and plain concrete. *Fracture Mechanics of concrete*, pages 171–225.
- Jansari, C., Kannan, K., Annabattula, R., Natarajan, S., et al. (2019). Adaptive phase field method for quasi-static brittle fracture using a recovery based error indicator and quadtree decomposition. *Engineering Fracture Mechanics*, 220:106599.

- Karma, A., Kessler, D. A., and Levine, H. (2001). Phase-field model of mode iii dynamic fracture. *Physical Review Letters*, 87(4):045501.
- Kiendl, J., Ambati, M., De Lorenzis, L., Gomez, H., and Reali, A. (2016). Phase-field description of brittle fracture in plates and shells. *Computer Methods in Applied Mechanics and Engineering*, 312:374–394.
- Kristensen, P. K. and Martínez-Pañeda, E. (2020). Phase field fracture modelling using quasi-newton methods and a new adaptive step scheme. *Theoretical and Applied Fracture Mechanics*, 107:102446.
- Kuhn, C. (2013). *Numerical and analytical investigation of a phase field model for fracture*.
- Kuhn, C. and Müller, R. (2008). A phase field model for fracture. *PAMM*, 8(1):10223–10224.
- Kuhn, C. and Müller, R. (2009). Phase field simulation of thermomechanical fracture. *PAMM*, 9(1):191–192.
- Kuhn, C. and Müller, R. (2011). A new finite element technique for a phase field model of brittle fracture. *Journal of Theoretical and Applied Mechanics*, 49(4):1115–1133.
- Kuhn, C., Schlüter, A., and Müller, R. (2015). On degradation functions in phase field fracture models. *Computational Materials Science*, 108:374–384.
- Landau, L. D., Lifshitz, E. M., and Pitaevskii, L. (1980). *Statistical physics, part i*.
- Lee, S., Mikelic, A., Wheeler, M. F., and Wick, T. (2018a). Phase-field modeling of two phase fluid filled fractures in a poroelastic medium. *Multiscale Modeling & Simulation*, 16(4):1542–1580.
- Lee, S., Min, B., and Wheeler, M. F. (2018b). Optimal design of hydraulic fracturing in porous media using the phase field fracture model coupled with genetic algorithm. *Computational Geosciences*, 22(3):833–849.
- Lee, S., Wheeler, M. F., and Wick, T. (2016). Pressure and fluid-driven fracture propagation in porous media using an adaptive finite element phase field model. *Computer Methods in Applied Mechanics and Engineering*, 305:111–132.
- Li, B., Peco, C., Millán, D., Arias, I., and Arroyo, M. (2015). Phase-field modeling and simulation of fracture in brittle materials with strongly anisotropic surface energy. *International Journal for Numerical Methods in Engineering*, 102(3-4):711–727.

- Liu, G., Li, Q., Msekh, M. A., and Zuo, Z. (2016). Abaqus implementation of monolithic and staggered schemes for quasi-static and dynamic fracture phase-field model. *Computational Materials Science*, 121:35–47.
- Ma, R. and Sun, W. (2020). Fft-based solver for higher-order and multi-phase-field fracture models applied to strongly anisotropic brittle materials. *Computer Methods in Applied Mechanics and Engineering*, 362:112781.
- Miehe, C., Aldakheel, F., and Raina, A. (2016). Phase field modeling of ductile fracture at finite strains: A variational gradient-extended plasticity-damage theory. *International Journal of Plasticity*, 84:1–32.
- Miehe, C., Hofacker, M., Schänzel, L.-M., and Aldakheel, F. (2015a). Phase field modeling of fracture in multi-physics problems. part ii. coupled brittle-to-ductile failure criteria and crack propagation in thermo-elastic–plastic solids. *Computer Methods in Applied Mechanics and Engineering*, 294:486–522.
- Miehe, C., Hofacker, M., and Welschinger, F. (2010a). A phase field model for rate-independent crack propagation: Robust algorithmic implementation based on operator splits. *Computer Methods in Applied Mechanics and Engineering*, 199(45):2765–2778.
- Miehe, C. and Mauthe, S. (2016). Phase field modeling of fracture in multi-physics problems. part iii. crack driving forces in hydro-poro-elasticity and hydraulic fracturing of fluid-saturated porous media. *Computer Methods in Applied Mechanics and Engineering*, 304:619–655.
- Miehe, C., Mauthe, S., and Teichtmeister, S. (2015b). Minimization principles for the coupled problem of darcy–biot-type fluid transport in porous media linked to phase field modeling of fracture. *Journal of the Mechanics and Physics of Solids*, 82:186–217.
- Miehe, C., Welschinger, F., and Aldakheel, F. (2014). Variational gradient plasticity at finite strains. part ii: Local–global updates and mixed finite elements for additive plasticity in the logarithmic strain space. *Computer Methods in Applied Mechanics and Engineering*, 268:704–734.
- Miehe, C., Welschinger, F., and Hofacker, M. (2010b). Thermodynamically consistent phase-field models of fracture: Variational principles and multi-field fe implementations. *International Journal for Numerical Methods in Engineering*, 83(10):1273–1311.
- Mikelić, A., Wheeler, M., and Wick, T. (2019). Phase-field modeling through iterative splitting of hydraulic fractures in a poroelastic medium. *GEM-International Journal on Geomathematics*, 10(1):2.

- Mikelić, A., Wheeler, M. F., and Wick, T. (2015). A phase-field method for propagating fluid-filled fractures coupled to a surrounding porous medium. *Multiscale Modeling & Simulation*, 13(1):367–398.
- Mikelić, A., Wheeler, M. F., and Wick, T. (2015a). Phase-field modeling of a fluid-driven fracture in a poroelastic medium. *Computational Geosciences*, 19(6):1171–1195.
- Mikelić, A., Wheeler, M. F., and Wick, T. (2015b). A quasi-static phase-field approach to pressurized fractures. *Nonlinearity*, 28(5):1371.
- Moës, N. and Belytschko, T. (2002). Extended finite element method for cohesive crack growth. *Engineering fracture mechanics*, 69(7):813–833.
- Moës, N., Dolbow, J., and Belytschko, T. (1999). A finite element method for crack growth without remeshing. *International journal for numerical methods in engineering*, 46(1):131–150.
- Moës, N., Stolz, C., Bernard, P.-E., and Chevaugeon, N. (2011). A level set based model for damage growth: the thick level set approach. *International Journal for Numerical Methods in Engineering*, 86(3):358–380.
- Msekh, M. A., Sargado, J. M., Jamshidian, M., Areias, P. M., and Rabczuk, T. (2015). Abaqus implementation of phase-field model for brittle fracture. *Computational Materials Science*, 96:472–484.
- Natarajan, S., Annabattula, R. K., et al. (2019). A fenics implementation of the phase field method for quasi-static brittle fracture. *Frontiers of Structural and Civil Engineering*, 13(2):380–396.
- Nguyen, T. T., Réthoré, J., and Baietto, M.-C. (2017). Phase field modelling of anisotropic crack propagation. *European Journal of Mechanics-A/Solids*, 65:279–288.
- Nguyen, V. P. and Wu, J.-Y. (2018). Modeling dynamic fracture of solids with a phase-field regularized cohesive zone model. *Computer Methods in Applied Mechanics and Engineering*, 340:1000–1022.
- Nguyena, V. P. and Wub, J.-Y. Modeling dynamic fracture of solids with a phase-field regularized cohesive zone model.
- Noii, N., Aldakheel, F., Wick, T., and Wriggers, P. (2020). An adaptive global–local approach for phase-field modeling of anisotropic brittle fracture. *Computer Methods in Applied Mechanics and Engineering*, 361:112744.

- Patil, R., Mishra, B., and Singh, I. (2018). An adaptive multiscale phase field method for brittle fracture. *Computer Methods in Applied Mechanics and Engineering*, 329:254 – 288.
- Peerlings, R., De Borst, R., Brekelmans, W., De Vree, J., and Spee, I. (1996). Some observations on localisation in non-local and gradient damage models. *European Journal of Mechanics A: Solids*, 15(6):937–953.
- Pillai, U., Triantafyllou, S. P., Essa, Y., and de la Escalera, F. M. (2020). An anisotropic cohesive phase field model for quasi-brittle fractures in thin fibre-reinforced composites. *Composite Structures*, 252:112635.
- Rabczuk, T. (2013). Computational methods for fracture in brittle and quasi-brittle solids: state-of-the-art review and future perspectives. *ISRN Applied Mathematics*, 2013.
- Rabczuk, T., Zi, G., Gerstenberger, A., and Wall, W. A. (2008). A new crack tip element for the phantom-node method with arbitrary cohesive cracks. *International Journal for Numerical Methods in Engineering*, 75(5):577–599.
- Reinoso, J., Paggi, M., and Linder, C. (2017). Phase field modeling of brittle fracture for enhanced assumed strain shells at large deformations: formulation and finite element implementation. *Computational Mechanics*, 59(6):981–1001.
- Ren, H., Zhuang, X., Anitescu, C., and Rabczuk, T. (2019). An explicit phase field method for brittle dynamic fracture. *Computers & Structures*, 217:45–56.
- Santillán, D., Juanes, R., and Cueto-Felgueroso, L. (2017). Phase field model of fluid-driven fracture in elastic media: Immersed-fracture formulation and validation with analytical solutions. *Journal of Geophysical Research: Solid Earth*, 122(4):2565–2589.
- Sargado, J. M., Keilegavlen, E., Berre, I., and Nordbotten, J. M. (2017). High-accuracy phase-field models for brittle fracture based on a new family of degradation functions. *Journal of the Mechanics and Physics of Solids*.
- Schillinger, D., Borden, M. J., and Stolarski, H. K. (2015). Isogeometric collocation for phase-field fracture models. *Computer Methods in Applied Mechanics and Engineering*, 284:583–610.
- Seleš, K., Lesičar, T., Tonković, Z., and Sorić, J. (2019). A residual control staggered solution scheme for the phase-field modeling of brittle fracture. *Engineering Fracture Mechanics*, 205:370–386.
- Shanthraj, P., Sharma, L., Svendsen, B., Roters, F., and Raabe, D. (2016). A phase field model for damage in elasto-viscoplastic materials. *Computer Methods in Applied Mechanics and Engineering*, 312:167–185.

- Shiozawa, S., Lee, S., and Wheeler, M. F. (2019). The effect of stress boundary conditions on fluid-driven fracture propagation in porous media using a phase-field modeling approach. *International Journal for Numerical and Analytical Methods in Geomechanics*, 43(6):1316–1340.
- Siegmund, T. and Brocks, W. (2000). A numerical study on the correlation between the work of separation and the dissipation rate in ductile fracture. *Engineering Fracture Mechanics*, 67(2):139–154.
- Strobl, M. and Seelig, T. (2015). A novel treatment of crack boundary conditions in phase field models of fracture. *PAMM*, 15(1):155–156.
- Strobl, M. and Seelig, T. (2016). On constitutive assumptions in phase field approaches to brittle fracture. *Procedia Structural Integrity*, 2:3705–3712.
- Tian, F., Tang, X., Xu, T., Yang, J., and Li, L. (2019). A hybrid adaptive finite element phase-field method for quasi-static and dynamic brittle fracture. *International Journal for Numerical Methods in Engineering*, 120(9):1108–1125.
- Ulmer, H., Hofacker, M., and Miehe, C. (2012). Phase field modeling of fracture in plates and shells. *PAMM*, 12(1):171–172.
- Ulmer, H., Hofacker, M., and Miehe, C. (2013). Phase field modeling of brittle and ductile fracture. *PAMM*, 13(1):533–536.
- Verhoosel, C. V. and de Borst, R. (2013). A phase-field model for cohesive fracture. *International Journal for numerical methods in Engineering*, 96(1):43–62.
- Vignollet, J., May, S., De Borst, R., and Verhoosel, C. V. (2014). Phase-field models for brittle and cohesive fracture. *Meccanica*, 49(11):2587–2601.
- Wang, Q., Feng, Y., Zhou, W., Cheng, Y., and Ma, G. (2020). A phase-field model for mixed-mode fracture based on a unified tensile fracture criterion. *Computer Methods in Applied Mechanics and Engineering*, 370:113270.
- Wheeler, M., Wick, T., and Wollner, W. (2014). An augmented-lagrangian method for the phase-field approach for pressurized fractures. *Computer Methods in Applied Mechanics and Engineering*, 271:69–85.
- Wick, T. (2016). Goal functional evaluations for phase-field fracture using pu-based dwr mesh adaptivity. *Computational Mechanics*, 57(6):1017–1035.

- Wick, T., Singh, G., Wheeler, M. F., et al. (2016). Fluid-filled fracture propagation with a phase-field approach and coupling to a reservoir simulator. *SPE Journal*, 21(3):981–999.
- Wu, J.-Y. (2017). A unified phase-field theory for the mechanics of damage and quasi-brittle failure. *Journal of the Mechanics and Physics of Solids*, 103:72–99.
- Wu, J.-Y. and Nguyen, V. P. (2018). A length scale insensitive phase-field damage model for brittle fracture. *Journal of the Mechanics and Physics of Solids*, 119:20–42.
- Xia, C.-C., Zhou, S.-W., Zhang, P.-Y., Hu, Y.-S., and Zhou, Y. (2015). Strength criterion for rocks subjected to cyclic stress and temperature variations. *Journal of Geophysics and Engineering*, 12(5):753.
- Yoshioka, K. and Bourdin, B. (2016). A variational hydraulic fracturing model coupled to a reservoir simulator. *International Journal of Rock Mechanics and Mining Sciences*, 88:137–150.
- Zhang, P., Hu, X., Wang, X., and Yao, W. (2018). An iteration scheme for phase field model for cohesive fracture and its implementation in abaqus. *Engineering Fracture Mechanics*, 204:268–287.
- Zhang, X., Sloan, S. W., Vignes, C., and Sheng, D. (2017). A modification of the phase-field model for mixed mode crack propagation in rock-like materials. *Computer Methods in Applied Mechanics and Engineering*, 322:123–136.
- Zhou, S. (2018). Fracture propagation in brazilian discs with multiple pre-existing notches by using a phase field method. *Periodica Polytechnica Civil Engineering*, 62(3):700–708.
- Zhou, S., Rabczuk, T., and Zhuang, X. (2018a). Phase field modeling of quasi-static and dynamic crack propagation: Comsol implementation and case studies. *Advances in Engineering Software*, 122:31–49.
- Zhou, S., Xia, C., Hu, Y., Zhou, Y., and Zhang, P. (2015a). Damage modeling of basaltic rock subjected to cyclic temperature and uniaxial stress. *International Journal of Rock Mechanics and Mining Sciences*, 77:163–173.
- Zhou, S., Xia, C., and Zhou, Y. (2018b). A theoretical approach to quantify the effect of random cracks on rock deformation in uniaxial compression. *Journal of Geophysics and Engineering*, 15(3):627.
- Zhou, S. and Zhuang, X. (2018). Adaptive phase field simulation of quasi-static crack propagation in rocks. *Underground Space*, pages –.

- Zhou, S. and Zhuang, X. (2020). Phase field modeling of hydraulic fracture propagation in transversely isotropic poroelastic media. *Acta Geotechnica*, pages 1–20.
- Zhou, S., Zhuang, X., and Rabczuk, T. (2018c). A phase-field modeling approach of fracture propagation in poroelastic media. *Engineering Geology*, 240:189–203.
- Zhou, S., Zhuang, X., and Rabczuk, T. (2019a). Phase field modeling of brittle compressive-shear fractures in rock-like materials: A new driving force and a hybrid formulation. *Computer Methods in Applied Mechanics and Engineering*, 355:729–752.
- Zhou, S., Zhuang, X., and Rabczuk, T. (2019b). Phase-field modeling of fluid-driven dynamic cracking in porous media. *Computer Methods in Applied Mechanics and Engineering*, 350:169–198.
- Zhou, S., Zhuang, X., and Rabczuk, T. (2020). Phase field method for quasi-static hydro-fracture in porous media under stress boundary condition considering the effect of initial stress field. *Theoretical and Applied Fracture Mechanics*, 107:102523.
- Zhou, S., Zhuang, X., Zhu, H., and Rabczuk, T. (2018d). Phase field modelling of crack propagation, branching and coalescence in rocks. *Theoretical and Applied Fracture Mechanics*, 96:174–192.
- Zhou, S.-W., Xia, C.-C., Du, S.-G., Zhang, P.-Y., and Zhou, Y. (2015b). An analytical solution for mechanical responses induced by temperature and air pressure in a lined rock cavern for underground compressed air energy storage. *Rock Mechanics and Rock Engineering*, 48(2):749–770.
- Zhou, S.-W., Xia, C.-C., Zhao, H.-B., Mei, S.-H., and Zhou, Y. (2017a). Numerical simulation for the coupled thermo-mechanical performance of a lined rock cavern for underground compressed air energy storage. *Journal of Geophysics and Engineering*, 14(6):1382.
- Zhou, S.-W., Xia, C.-C., Zhao, H.-B., Mei, S.-H., and Zhou, Y. (2017b). Statistical damage constitutive model for rocks subjected to cyclic stress and cyclic temperature. *Acta Geophysica*, 65(5):893–906.
- Zhuang, X., Augarde, C., and Bordas, S. (2011). Accurate fracture modelling using meshless methods, the visibility criterion and level sets: formulation and 2d modelling. *International Journal for Numerical Methods in Engineering*, 86(2):249–268.
- Zhuang, X., Augarde, C., and Mathisen, K. (2012). Fracture modeling using meshless methods and level sets in 3d: framework and modeling. *International Journal for Numerical Methods in Engineering*, 92(11):969–998.

Zhuang, X., Zhou, S., Sheng, M., and Li, G. (2020). On the hydraulic fracturing in naturally-layered porous media using the phase field method. *Engineering Geology*, 266:105306.